Optical Measurements of Spin/Valley Polarization in Transition Metal Dichalcogenides

by

Xinlin Song

A dissertation submitted in partial fulfillment
of the requirements for the degree of
Doctor of Philosophy
(Applied Physics)
in The University of Michigan
2018

Doctoral Committee:

Associate Professor Vanessa Sih, Chair
Professor Cagliyan Kurdak
Professor Theodore B. Norris
Associate Professor Kai Sun
Assistant Professor Liuyan Zhao

Xinlin Song

xinlins@umich.edu

ORCID iD: 0000-0002-1452-0803

TABLE OF CONTENTS

LIST OF FIGURES

Figure

ABSTRACT

Finding a fundamentally novel way to generate and store information is one of the most critical topics in semiconductor research during the past several decades. Spin electronics (spintronics), using the spin degree of freedom to store and transfer information in solid state devices, offers one possible solution. In this dissertation, we use optical ways to study the spin dynamics in semiconductors which includes generating/detecting spin polarization and measuring spin lifetime.

Monolayer transition metal dichalcogenides (TMDs), a category of direct bandgap semiconductors, are great candidates for spintronics devices due to their unique optical properties and a new degree of freedom called valley pseudospin. We use optical orientation to generate spin/valley polarization in monolayer tungsten diselenide WSe_2 and measure its lifetime. A very long $\sim$ 80 ns spin/valley polarization lifetime is observed which is much longer than the radiative recombination time. We propose two possible physical mechanisms for this long-lived polarization. In the single particle picture, this long-lived polarization signal can be explained by the transfer of polarization from photo-excited carriers to resident carriers. Alternatively, in the quasi-particle picture, it can be attributed to the dark trions, which cannot radiatively recombine due to spin or momentum mismatch. Also, the spin/valley polarization is insensitive to an external transverse magnetic field because of the large spin splitting in the valence band. We also find that the excitation energy that maximizes the

Kerr rotation follows the free exciton emission energy, although the localized exciton emission dominates the photoluminescence spectrum at low temperature.

To study the spin/valley polarization transport in TMDs, such as spin diffusion length and spin/valley Hall effect, a high-resolution (3-micron resolution) time-resolved Kerr rotation microscope (TRKM) has been designed and built. The Kerr rotation microscope has a 4-f scanning system which allows us to do a relatively large spatial scan with a fine spatial resolution. Test measurements on bulk GaAs and InGaAs samples show high signal-to-noise data on the TRKM setup.

CHAPTER I

Introduction and Organization

Electron spin is an intrinsic form of angular momentum which was first demonstrated by Otto Stern and Walther Gerlach in their famous experiment in 1922 [1]. A natural question people have is whether electron spin can be used as an information carrier for spin-based solid-state devices. Spintronics, starting around the 1980s, is a multidisciplinary field whose central theme is the active manipulation of the spin degree of freedom in solid-state systems[2]. One essential breakthrough in spintronics is the giant magnetoresistance (GMR) effect discovered by Albert Fert and Peter Grunberg in 1988 [3, 4]. GMR is a quantum mechanical effect observed in layered magnetic thin-film structures that are composed of alternating layers of ferromagnetic and nonmagnetic layers [5]. Due to spin-dependent scattering, the resistance of the material can be tuned by changing the relative magnetization direction of the ferromagnetic layers. GMR-based spintronic devices such as high-frequency read head and nonvolatile random access memory have been designed and are now widely used [6, 7].

Although metal-based spintronic devices have made significant progress in building spin valves and switches, they cannot amplify the signal. Therefore it is hard to construct fully-functional spintronic circuits with ferromagnetic or antiferromagnetic materials. However, semiconductor-based spintronic devices could in principle pro-

vide amplification and serve as multi-functional devices. More importantly, it would be much easier for semiconductor-based devices to be integrated with traditional semiconductor manufacturing technology [8]. The study of generating, manipulating and detecting spin in semiconductors has attracted a lot of research attention in the past twenty years.

My PhD study focuses on using light to generate and detect electron spin polarization in a category of novel semiconductors: transition metal dichalcogenides. In Chapter II, a brief introduction to optical spin orientation is presented followed by commonly observed spin relaxation mechanisms in semiconductors. In Chapter IV, I will introduce the indirect-direct bandgap transition, optical selection rules and exciton states in transition metal dichalcogenides. In Chapter III, I will discuss the frequently-used experimental techniques in my study which includes time-resolved Faraday/Kerr rotation, resonant spin amplification and optical modulation. In Chapter V, I will focus on the long-lived spin/valley polarization in monolayer tungsten diselenide WSe_2, which is robust to an external transverse magnetic field and decreases with increasing temperature. Two possible physical origins for the long-lived polarization, resident holes and dark trions, are discussed. To study spin transport and diffusion in transition metal dichalcogenides, a high resolution time-resolved Kerr rotation microscope (TRKM) is designed and built. In Chapter VI, an overview of the TRKM setup is presented, followed by test measurement results. Then we discuss how the measurement geometry (transmission or reflection) could affect the measured spin lifetime. Chapter VII concludes the dissertation.

CHAPTER II

Optical Properties and Spin Dynamics in Semiconductors

2.1 Optical Orientation

In certain semiconductors, due to the optical selection rules, circularly polarized light can generate different amounts of spin-up and spin-down electrons (holes) creating spin polarization. We first show the theoretical derivation of the spin polarization generation efficiency in GaAs which is representative of a large class of III-V and II-VI zinc-blende semiconductors. Then the optical selection rules of 2D transition metal dichalcogenides are shown.

2.1.1 Optical Selection Rules in GaAs

GaAs is a direct bandgap (E_g = 1.52 eV at T = 0 K) semiconductor with its bandedge located at the Γ point. The conduction band edge is S-like. The valence band contains three sub-bands: the heavy hole band, light hole band, and spin-orbit split-off band. The heavy hole and light hole band overlap at the Γ point and the spin-orbit split-off band sits Δ_{so} lower than the heavy and light hole bands, where Δ_{so} is the spin-orbit splitting. The schematic band structure of GaAs is shown in Figure (2.1).

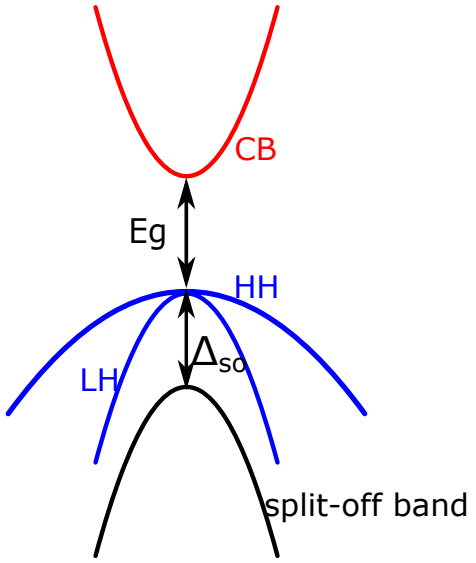

Figure 2.1: Schematic band structure of GaAs. The conduction band (CB) is s-like. The heavy hole (HH) and light hole (LH) band overlap at the Γ point. The spin-orbit split-off band sits Δ_{so} below the Γ point.

Because of spin-orbit coupling, the eigenstates of the system are represented using the total angular momentum and its projection along the z-axis: $|J, m_j\rangle$. $J = \frac{1}{2}$ for both the conduction band and the spin-orbit split-off band. $J = \frac{3}{2}$ for the valence band with $m_j = \pm\frac{3}{2}$ the heavy hole band and $m_j = \pm\frac{1}{2}$ the light hole band. $|J, m_j\rangle$ can be represented using s and p orbital wave functions $|S\rangle, |X\rangle, |Y\rangle, |Z\rangle$ and the spin states $|\uparrow\rangle, |\downarrow\rangle$. The wave functions of electrons at the gamma point for the conduction band and the valence bands are listed in the Table (2.1):

symmetry	$\|J, m_j\rangle$	wave function
Γ_6	$\|\frac{1}{2}, \frac{1}{2}\rangle$	$\|S\uparrow\rangle$
	$\|\frac{1}{2}, -\frac{1}{2}\rangle$	$\|S\downarrow\rangle$
Γ_7	$\|\frac{1}{2}, \frac{1}{2}\rangle$	$\|-(\frac{1}{3})^{1/2}[(X+iY)\downarrow -Z\uparrow]\rangle$
	$\|\frac{1}{2}, -\frac{1}{2}\rangle$	$\|-(\frac{1}{3})^{1/2}[(X+iY)\downarrow +Z\uparrow]\rangle$
Γ_8	$\|\frac{3}{2}, \frac{3}{2}\rangle$	$\|(\frac{1}{2})^{1/2}(X+iY)\uparrow\rangle$
	$\|\frac{3}{2}, \frac{1}{2}\rangle$	$\|(\frac{1}{6})^{1/2}[(X+iY)\downarrow +2Z\uparrow]\rangle$
	$\|\frac{3}{2}, \frac{1}{2}\rangle$	$\|-(\frac{1}{6})^{1/2}[(X-iY)\uparrow -2Z\downarrow]\rangle$
	$\|\frac{3}{2}, -\frac{3}{2}\rangle$	$\|(\frac{1}{2})^{1/2}(X-iY)\downarrow\rangle$

Table 2.1: Electron wave functions of GaAs at the band edge.

The transition probability between two arbitrary states $|a\rangle$ and $|b\rangle$ can be calculated by evaluating the matrix element $\langle a|\, D\, |b\rangle$, where D is the dipole operator. For circularly polarized light along the z-axis, $D \sim Y_1^{\pm 1}$, where Y_l^m are spherical harmonics.

For example, the matrix element between conduction band state $|\frac{1}{2}, \frac{1}{2}\rangle$ and heavy hole valence band state $|\frac{3}{2}, \frac{3}{2}\rangle$ is (with σ^- light):

$$\begin{aligned}
\langle \frac{1}{2}, \frac{1}{2}|\, Y_1^{-1}\, |\frac{3}{2}, \frac{3}{2}\rangle &= R\,(\frac{1}{2})^{1/2}\, \langle S\uparrow|\, Y_1^{-1}\, |(X+iY)\uparrow\rangle \\
&= R\,(\frac{1}{2})^{1/2}\, \langle Y_0^0|\, Y_1^{-1}\, |2^{1/2} Y_1^1\rangle \\
&= -\frac{R}{\sqrt{4\pi}}
\end{aligned} \tag{2.1}$$

where R is the radial part of the wave function, which is the same for all the transition matrix between the conduction band and the heavy, light hole valance band. It will be canceled out when calculating the spin polarization.

The matrix element between conduction band state $|\frac{1}{2}, -\frac{1}{2}\rangle$ and light hole valence band state $|\frac{3}{2}, \frac{1}{2}\rangle$ is:

$$\begin{aligned}
\langle \frac{1}{2}, -\frac{1}{2}|\, Y_1^{-1}\, |\frac{3}{2}, \frac{1}{2}\rangle &= R\,(\frac{1}{6})^{1/2}\, \langle S\downarrow|\, Y_1^{-1}\, |(X+iY)\downarrow + 2Z\uparrow\rangle \\
&= R\,(\frac{1}{6})^{1/2}\, \langle S\downarrow|\, Y_1^{-1}\, |(X+iY)\downarrow\rangle \\
&= R\,(\frac{1}{6})^{1/2}\, \langle Y_0^0|\, Y_1^{-1}\, |2^{1/2} Y_1^1\rangle \\
&= -\frac{R}{\sqrt{12\pi}}
\end{aligned} \tag{2.2}$$

Therefore the population ratio between state $|\frac{1}{2}, \frac{1}{2}\rangle$ and $|\frac{1}{2}, -\frac{1}{2}\rangle$ is (using σ^- light):

$$\frac{n_\uparrow}{n_\downarrow} = \frac{|\,\langle \frac{1}{2}, \frac{1}{2}|\, Y_1^{-1}\, |\frac{3}{2}, \frac{3}{2}\rangle\,|^2}{|\,\langle \frac{1}{2}, -\frac{1}{2}|\, Y_1^{-1}\, |\frac{3}{2}, \frac{1}{2}\rangle\,|^2} = 3 \tag{2.3}$$

The spin polarization is:

$$\frac{n_\uparrow - n_\downarrow}{n_\uparrow + n_\downarrow} = 50\% \tag{2.4}$$

The transition rate between all the possible conduction band and valence band states are shown in Figure (2.2):

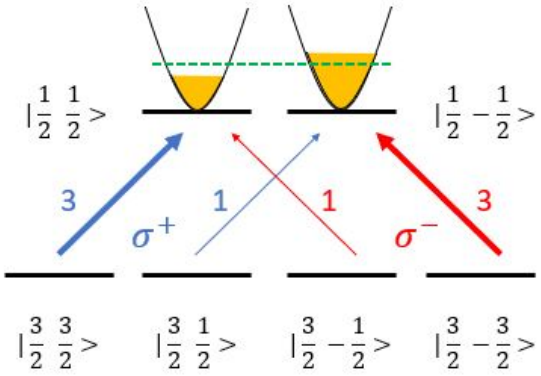

Figure 2.2: Optical selection rules of GaAs. The transition rate and the helicity of the corresponding light are also shown. The electron population of the spin-up and spin-down states is represented by the yellow area.

Once the spin polarization is created, the absorption curve of the σ^+ and σ^- light will shift. In Figure (2.2), the spin-down population is greater than that of spin-up. Suppose the incident photons have energy indicated by the green dash line. No more electrons can be generated to state $|\frac{1}{2}, -\frac{1}{2}\rangle$ because of the Pauli exclusion principle. Only state $|\frac{1}{2}, \frac{1}{2}\rangle$ is available. Because of the optical selection rule, σ^+ light is absorbed three times more than σ^- light. This absorption curve shift gives rise to Faraday/Kerr rotation which will be covered in Chapter IV.

2.2 T_1 and T_2

There are two quantities used to describe how fast the spin polarization changes with time. T_1 is the spin relaxation time which describes how fast the spin polarization reaches equilibrium. T_2 is the spin dephasing time which captures how long it takes

for the system to lose phase coherence. We first explain the difference between T_1 and T_2 from both microscopic and macroscopic perspectives.

In a two-state system (microscopic perspective), suppose there is a population difference between the spin-up and spin-down states. T_1 is the time it takes for the system to reach the population equilibrium. Whereas T_2 captures the time the two states lose coherence. For example, the system starts with a superposition of the spin-up and spin-down states, i.e., $\phi = \frac{1}{\sqrt{2}}(\langle\uparrow| + \langle\downarrow|)$. After T_2 time, the coherence between the spin-up and spin-down is lost and the state ϕ no longer exists. The population of the spin-up and spin-down state do not change during the T_2 period.

T_1 and T_2 are also used on an ensemble of spins (macroscopic perspective). Instead of having clear physical meaning as in the microscopic case, T_1 and T_2 are phenomenological parameters. The definition of T_1 and T_2 are through the Bloch-Torrey equations (for simplicity we don't include the diffusion term):

$$\begin{aligned}
\frac{\partial M_x}{\partial t} &= \gamma(\mathbf{M} \times \mathbf{B})_x - \frac{M_x}{T_2} \\
\frac{\partial M_y}{\partial t} &= \gamma(\mathbf{M} \times \mathbf{B})_y - \frac{M_y}{T_2} \\
\frac{\partial M_z}{\partial t} &= \gamma(\mathbf{M} \times \mathbf{B})_z - \frac{M_z - M_z^0}{T_1}
\end{aligned} \tag{2.5}$$

where $\mathbf{B} = B_0\hat{z} + \mathbf{B}(t)$, the magnetic field has a constant component along the z-axis and a time dependent component in the x-y plane. $\gamma = \frac{\mu_B g}{\hbar}$ is the gyromagnetic ratio, and $M_z^0 = \chi B_0$ is the steady state magnetization. Because of Eq (2.5), T_1 and T_2 are also called longitudinal and transverse magnetization decay time respectively.

In the macroscopic scenario, T_1 describes the time it takes for the magnetization to go back to equilibrium. This usually involves energy transfer from the spin ensemble to the crystal lattice. T_2 is the time it takes for an ensemble of transverse spins, initially precessing in phase, to lose their phase due to different g-factors or the

fluctuation of the spin-orbit field. For electrons in the conduction band, T_1 and T_2 are usually close [2].

2.3 Spin Relaxation Mechanisms

2.3.1 D'yakonov-Perel Mechanism

D'yakonov-Perel spin relaxation stems from spin-orbit coupling in materials that lack spatial inversion symmetry. The spatial inversion asymmetry can either be due to the different atoms in the Bravais lattice (such as GaAs) or the structure of the sample (such as in a heterostructure). Without the spatial inversion symmetry[1], the state for momentum **k** and -**k** are no longer degenerate:

$$E_{\mathbf{k}\uparrow} \neq E_{-\mathbf{k}\uparrow} \tag{2.6}$$

The time-reversal symmetry still holds:

$$E_{\mathbf{k}\uparrow} = E_{-\mathbf{k}\downarrow} \tag{2.7}$$

Combining equation (2.6) and equation (2.7), we have:

$$E_{\mathbf{k}\uparrow} \neq E_{\mathbf{k}\downarrow} \tag{2.8}$$

Eq (2.8) tells us that the spin-up and spin-down states are no longer degenerate. In others words, in samples without spatial inversion symmetry, there is an internal magnetic field $\mathbf{B}_i(\mathbf{k})$, and this magnetic field is **k** dependent. $\mathbf{B}_i(\mathbf{k})$ causes spin to precess with Larmor precession frequency $\mathbf{\Omega}(\mathbf{k}) = \frac{e}{m}\mathbf{B}_i(\mathbf{k})$. This **k** dependent precession frequency results in the D'yakonov-Perel relaxation.

We first consider one single spin. Assume the momentum scattering time is τ_m

[1]Since $\frac{d\mathbf{r}}{dt}=\frac{\hbar\mathbf{k}}{m}$, changing **r** to -**r** changes **k** to -**k**. Also when change t to -t, **k** flips sign.

and the electron is at state $\mathbf{k}$. The change of the spin direction because of $\mathbf{\Omega}(\mathbf{k})$ is [2]:

$$\mathbf{S}(t+\tau_m) - \mathbf{S}(t) = \mathbf{\Omega}(\mathbf{k}) \times \mathbf{S}(t)\tau_m \tag{2.9}$$

When momentum scattering happens, the electron is scattered from state $\mathbf{k}$ to state $\mathbf{k}'$. The change of spin direction due to $\mathbf{\Omega}(\mathbf{k}')$ is:

$$\mathbf{S}(t+2\tau_m) - \mathbf{S}(t+\tau_m) = \mathbf{\Omega}(\mathbf{k}') \times \mathbf{S}(t+\tau_m)\tau_m \tag{2.10}$$

Combining Eq (2.9) and Eq (2.10), we have:

$$\mathbf{S}(t+2\tau_m) - \mathbf{S}(t) = \mathbf{\Omega}(\mathbf{k}) \times \mathbf{S}(t)\tau_m + \mathbf{\Omega}(\mathbf{k}') \times \mathbf{S}(t+\tau_m)\tau_m \tag{2.11}$$

Since the momentum scattering is random, the spin precesses along a random internal magnetic field. Now consider n successive scattering events. Eq 2.11 can be generalized to:

$$\mathbf{S}(t+n\tau_m) - \mathbf{S}(t) = \sum_{i=1}^{n} \mathbf{\Phi}_i \tag{2.12}$$

where $\mathbf{\Phi}_i$ is the spin phase change between the (i-1)-th and the i-th scattering event. Since $\mathbf{\Phi}_i$ is a random variable, Eq (2.12) can be interpreted as a random walk. Consider a time period Δt, during which the number of steps of the random walk is $\frac{\Delta t}{\tau_m}$, the root-mean-square deviation of the spin from its original direction can roughly be written as[3]:

[2]Here we assume $\tau_m \ll \frac{1}{\bar{\Omega}}$, where $\bar{\Omega} = \int p(k)|\Omega(k)|dk$ is the average precession frequency over the momentum space.

[3]In a random walk, the root mean square distance is proportional to the square root of the number of steps.

$$\begin{aligned}\sqrt{\overline{(\mathbf{S}(t+\Delta t)-\mathbf{S}(t))^2}} &\approx \sqrt{\frac{\Delta t}{\tau_m}}|\mathbf{\Phi}| \\ &\approx \sqrt{\frac{\Delta t}{\tau_m}}\bar{\Omega}\tau_m\end{aligned} \tag{2.13}$$

where $\bar{\Omega}$ is the averaged precession frequency over the momentum space. $\bar{\Omega}\tau_m$ is the mean phase change between two scattering events. Define the spin lifetime τ_s such that $\sqrt{\overline{(\mathbf{S}(t+\Delta t)-\mathbf{S}(t))^2}} = 1$. Using equation (2.13), we have:

$$\begin{aligned}1 &= \frac{\tau_s}{\tau_m}\bar{\Omega}^2\tau_m^2 \\ \rightarrow \tau_s &= \frac{1}{\bar{\Omega}^2\tau_m}\end{aligned} \tag{2.14}$$

If we start with an ensemble of spins, because of the random precession, the spin ensemble will dephase. The spin lifetime is described by Eq (2.14) which is inversely proportional to the momentum scattering time τ_m. The faster the momentum scattering, the longer the spin lifetime. However, one has to bear in mind that all the derivation is in the scenario $\tau_m \ll \frac{1}{\bar{\Omega}}$. In other words, the momentum scattering is much faster than the precession. When $\tau \approx \frac{1}{\bar{\Omega}}$, the spin ensemble already lost phase information before momentum scattering. Eq (2.14) no longer holds.

Figure (2.3) shows the simulation results of the D'yakonov-Perel mechanism. The initial direction of all the spins is pointing to the north pole of the Bloch sphere. Each spin precesses along an internal magnetic field, which is momentum dependent. Every time the spin gets scattered, the direction of the internal magnetic field changes (for simplicity, the magnitude is fixed). In Figure (2.3) (a)(b), $\tau_m\bar{\Omega} = 0.02 \ll 1$ the condition of D'yakonov-Perel mechanism holds and the spin lifetime is inversely proportional to the momentum scattering time. The larger the momentum scattering rate, the less the dephasing. In Figure (2.3) (c)(d), $\tau_m\bar{\Omega} = 0.1 \approx 1$ the condition of

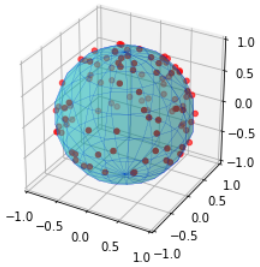

(a) $\frac{1}{\tau_m} = \infty$, $\tau_m\bar{\Omega} = 0.02$, steps=100

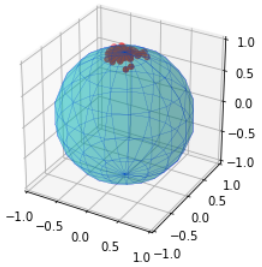

(b) $\frac{1}{\tau_m} = 0.9$, $\tau_m\bar{\Omega} = 0.02$, steps=100

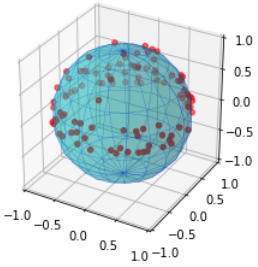

(c) $\frac{1}{\tau_m} = \infty$, $\tau_m\bar{\Omega} = 0.1$, steps=10

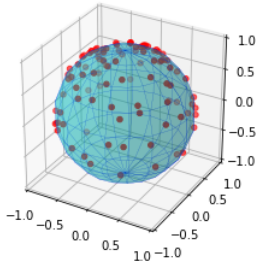

(d) $\frac{1}{\tau_m} = 0.9$, $\tau_m\bar{\Omega} = 0.1$, steps=10

Figure 2.3: Simulation of D'yakonov-Perel mechanism. Each red point represents one spin on the Bloch sphere (100 spins in total). The number of steps corresponds to the number of scattering events. (a) and (b) show that when the precession rate is much slower than the momentum scattering rate, the spin ensemble dephases faster for slower momentum scattering rate. (c) and (d) show that when the precession rate is comparable to the momentum scattering rate, DP mechanism no longer holds.

D'yakonov-Perel mechanism no longer holds and Eq (2.3) is no longer true.

2.3.2 Elliot-Yafet mechanism

In the presence of the spin-orbit interaction

$$V_{so} = \frac{\hbar}{4m^2c^2}\nabla V_{sc} \times \hat{\mathbf{p}} \cdot \hat{\sigma} \tag{2.15}$$

where m is the free electron mass, V_{sc} is the scalar periodic potential from the lattice, $\hat{\mathbf{p}} = -i\hbar\nabla$ is the momentum operator and $\hat{\sigma}$ are the Pauli matrices, the Bloch wave is no longer the eigenstate of the Pauli matrices. The eigenstates of the

Hamiltonian are a mix of spin-up and spin-down states [9]:

$$\Psi_{\mathbf{k}n\uparrow}(\mathbf{r}) = [a_{\mathbf{k}n}(\mathbf{r})\,|\uparrow\rangle + b_{\mathbf{k}n}(\mathbf{r})\,|\downarrow\rangle]e^{\mathbf{k}\cdot\mathbf{r}} \tag{2.16}$$

$$\Psi_{\mathbf{k}n\downarrow}(\mathbf{r}) = [a^{\star}_{-\mathbf{k}n}(\mathbf{r})\,|\downarrow\rangle - b^{\star}_{-\mathbf{k}n}(\mathbf{r})\,|\uparrow\rangle]e^{\mathbf{k}\cdot\mathbf{r}} \tag{2.17}$$

where $\mathbf{k}$ is the lattice momentum, n is the band index. Using perturbation theory, we know that

$$|b| \approx \frac{\lambda_{so}}{\Delta E} << 1 \tag{2.18}$$

where λ_{so} is the amplitude of the matrix element of V_{so} between the two states and ΔE is the energy between the band state in question and the state in the nearest band with the same momentum. This means that although the eigenstates are a mix of the spin-up and spin-down states, one component dominates. This is why in Eq (2.16) and Eq (2.17), we still use spin-up and spin-down to denote the states on the left side of the equations.

Since the Bloch state and the spin state are coupled together, momentum scattering can lead to spin scattering. Let V_i be the momentum scattering interaction. The spin relaxation rate is $\frac{1}{\tau_s} = |(\Psi_{\mathbf{k}n\uparrow}, V_i\Psi_{\mathbf{k}'n'\downarrow})|^2$ and the momentum scattering rate is $\frac{1}{\tau_m} = |(\Psi_{\mathbf{k}n\uparrow}, V_i\Psi_{\mathbf{k}'n'\uparrow})|^2$. Using Eq (2.16) and Eq (2.17), we have:

$$\frac{1}{\tau_s} \approx \frac{|b|^2}{\tau_m} \tag{2.19}$$

Although Eq (2.19) gives the relation between τ_s and τ_m, $|b|^2$ is not a parameter that can be measured directly from experiment. However, the Elliot relation relates τ_s to Δg which is the difference between the electron g-factor in the semiconductor and the free electron g-factor. Δg can be measured directly from experiments. The

Elliot relation is as follows:

$$\frac{1}{\tau_s} \approx \frac{(\Delta g)^2}{\tau_m} \tag{2.20}$$

The derivation of Eq (2.20) can be found in Elliott's original paper [9].

The Yafet relation connects the temperature dependence of T_1 with that of resistivity ρ by realizing $\frac{1}{\tau_m} \propto \rho$:

$$\frac{1}{T_1} \approx \frac{|b|^2}{\tau_m} = |b^2|\rho(T) \tag{2.21}$$

Yafet proved that at low temperature [10]:

$$\frac{1}{T_1} \propto T^5 \tag{2.22}$$

In III-V semiconductors, the spin relaxation rate of conduction electrons with energy $E_{\mathbf{k}}$ can be written as [11, 12]:

$$\frac{1}{\tau_s(E_{\mathbf{k}})} = A(\frac{\Delta_{so}}{E_g + \Delta_{so}})^2(\frac{E_{\mathbf{k}}}{E_g})\frac{1}{\tau_q(E_{\mathbf{k}})} \tag{2.23}$$

where Δ_{so} is the spin splitting of the valence band and E_g is the band gap, and A is a numerical factor of order 1. The actual value of A depends on the specific momentum scattering mechanism (charge or neutral impurity, phonon, electron-hole). From Eq (2.23), we know that Elliot-Yafet mechanism is important for materials with small bandgap and large valance spin splitting.

In summary, the D'yakonov-Perel mechanism and Elliott-Yafet mechanism have different dependence on momentum scattering rate. Both these two mechanisms coexist in systems lacking inversion symmetry. The relative strength of these two depends on a lot of factors and is case dependent. However, the most important trend is that the D'yakonov-Perel mechanism becomes essential with increasing bandgap

and increasing temperature [2].

CHAPTER III

Introduction to Transition Metal Dichalcogenides

3.1 Indirect-Direct Bandgap Transition

Some transition metal dichalcogenides (TMDs) are semiconductors with a bandgap between 1-2 eV[1]. The chemical formula of these TMDs is MX_2, where M can be Mo, W and X can be S, Se and Te. Similar to graphite, bulk TMDs have layered structure, and the layers are held together by Van der Waals force. The weak Van der Waals interactions between the layers make it possible to make monolayer TMDs using "Scotch tape method". The crystal structure of the monolayer TMD is shown in Figure (3.1).

Although bulk TMDs are indirect bandgap semiconductors, as the number of layers decreases, the conduction band and valence band edge shift and finally become direct bandgap for monolayer [14]. Theoretical calculations pointed out that the direct bandgap in monolayer TMDs is located at the corners of the hexagonal Brillouin zone, i.e., at the K and K′ points [15]. Figure (3.2) (a) shows the first-principles calculations results of the bandgap versus number of layers in MoS_2. Both the conduction band and valence band edge are at the K point when the number of layers n=1. For n>1, the conduction band edge is still at K point while the valence band edge shifts to the

[1]Rigorously speaking, this energy is the resonant excitation energy. The real bandgap is between 2-3 eV. Since the exciton binding energy is very large (0.5 - 1 eV) in monolayer TMDs, electrons and holes form excitons. The excitons can be generated with energy much lower than the bandgap.

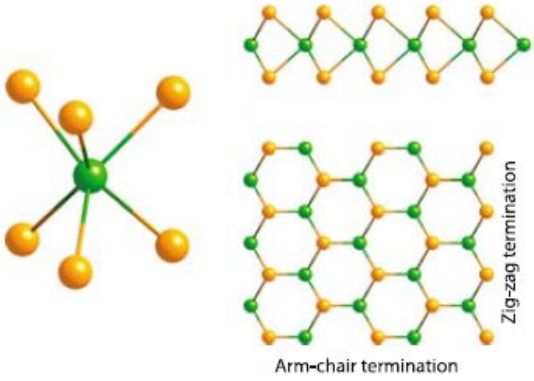

Figure 3.1: Crystal structure of the monolayer TMDs [13]. Metal atoms are shown in green and chalcogen atoms are shown in orange. Left: trigonal prismatic coordination geometry. Upper right: side view of the monolayer TMDs. Lower right: top view of the monolayer TMDs.

Γ point.

The calculation matches the experimental results well. Figure (3.2) (b) shows the mono- and bilayer MoS_2 PL emission intensity. The monolayer has a much stronger emission peak than the bilayer, supporting the indirect-direct bandgap transition predicted by theory.

3.2 Valley/Spin-Dependent Optical Selection Rules

The spatial inversion symmetry breaking in monolayer TMDs leads to valley-dependent optical selection rules, i.e. the K (K′) valley only couples to right circularly polarized σ^+ (left circularly polarized σ^-) light [17]. While the symmetry derivation is only applicable at the high symmetry point K and K′, first-principles calculations have shown that the selection rules, in fact, hold approximately true in a large neighborhood of the K and K′ points [18]. This makes it possible to selectively generate carriers in the K and K′ valley with optical orientation.

In addition to spatial inversion symmetry breaking, monolayer TMDs have strong spin-orbit coupling (SOC) due to the transition metals, which results in spin splitting.

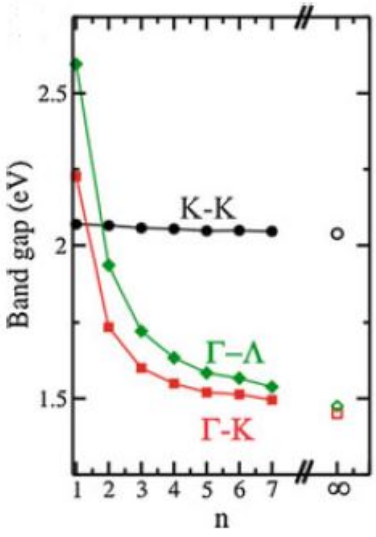

(a) Engery differences between the high symmetry points versus the number of layers (n) in MoS_2 from first-principles calculations [15].

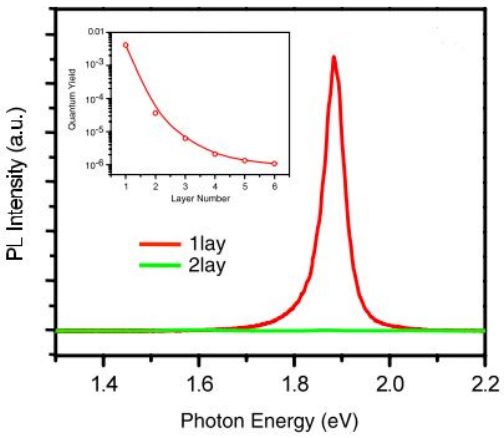

(b) PL spectra of mono- and bilayer MoS_2 samples. Inset: PL quantum yield of thin layers for n = 1 to 6 [16].

Figure 3.2: Indirect-direct bandgap transition of MoS_2

The spin splitting in the conduction band is a few to tens of meV ($\sim$ 1 meV for MoX_2, and $\sim$ 30 meV for WX_2) and that of valence band is hundreds of meV ($\sim$ 150 meV for MoX_2, and $\sim$ 400 meV for WX_2) [17, 19]. On the other hand, time reversal symmetry requires the spin splitting at different valleys to have different signs. At the K valley the spin-up valence band has higher energy than the spin-down valence band while at the K′ valley, the spin-down band has higher energy than the spin-up band[2]. Thus the valley index and the spin orientation are inter-locked and the valley-dependent optical selection rule becomes spin-dependent. Circularly polarized light generates valley and spin polarization simultaneously. Figure (3.3) shows the schematic band structure and optical selection rules of monolayer WSe_2. When the excitation energy is close to the resonant excitation energy, σ^+ excitation generates spin-up electron and hole pairs (excitons) in the K valley and σ^- excitation generates spin-down electron

[2]The spin-splitting in the conduction band and the valence band have the same sign in Tungsten based TMDs whereas in Molybdenum based TMDs the sign is different.

and hole pairs (excitons) in the K′ valley. Theoretically, the valley/spin polarization is 100%.

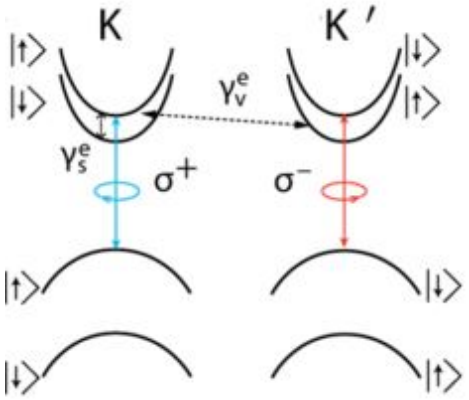

Figure 3.3: Schematic band structure along with the valley optical selection rules and electron scattering processes for monolayer WSe_2. Both the conduction band and valence band spin splittings are shown. γ_v^e and γ_s^e are the electron phonon-assisted intervalley scattering rate (preserves spin) and intravalley scattering rate (flips spin) respectively.

The valley/spin optical selection rules can be verified through polarization resolved photoluminescence (PL) measurements [20, 21] where the monolayer TMDs is excited using circularly polarized light. The polarization of the emission is calculated via: $P = \frac{I(\sigma^+)-I(\sigma^-)}{I(\sigma^+)+I(\sigma^-)}$, where $I(\sigma^+)$ and $I(\sigma^-)$ are the intensity of σ^+ and σ^- emission respectively. Because of valley-dependent optical selection rules, only a particular valley is excited. In the case when the photo-recombination time is shorter than the inter-valley scattering time, the PL emission helicity is the same as the excitation(The polarization P is 100%). Figure (3.4) shows the polarization resolved PL with σ^+ and σ^- excitation. The PL polarization emission changes sign when the excitation helicity changes [20].

3.3 Exciton in 2D TMDs

An exciton is a bound state formed by an excited electron and hole due to Coulomb attraction [22]. Based on the radius and the binding energy of the excitons, they can

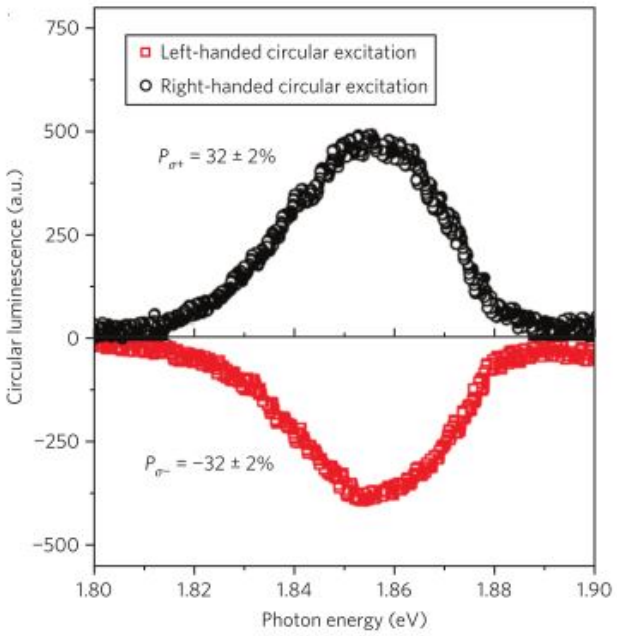

Figure 3.4: A polarization resolved luminescence spectra under circularly polarized excitation from a He-Ne laser at 1.96 eV and 10 K. Circularly polarized light is observed along the out-of-plane direction of a MoS_2 monolayer with right- and left-handed circular excitation respectively [20].

be divided into two categories. In materials with small dielectric constant such as ionic crystals, the electron and hole are tightly bound to each other within the same or nearest neighbor unit cells. Such excitons are called Frenkel excitons and have typical binding energies on the order of 0.1-1 eV. On the other hand, in semiconductors, the dielectric constant is large. The Coulomb interaction is reduced due to the valence band electron screening, which results in a much larger exciton radius than the lattice spacing. This kind of excitons is called Wannier excitons. For example, in GaAs, the exciton binding energy is about 4.7 meV, and the Bohr radius is about 12 nm [23].

In addition to dielectric constant, the dimension of the material also affects the exciton binding energy. Intuitively, the lower the dimension, the smaller the screening effect. Concretely, the exciton binding energy decreases by a factor of 4 from 3D to 2D

[24]. Also, for monolayer samples, part of the electric field lines are not confined within the materials, experiencing the vacuum permittivity [25], which further increases the exciton binding energy. Theoretical calculations show that the binding energy of excitons in MoS_2 is about 0.9 eV with Bohr radius of 0.93 nm [26].

Because of the strong Coulomb interaction, in TMDs, the optical response is dominated by excitonic states within the bandgap. Therefore, the band-to-band transition peak does not show up in the PL spectra. Instead, two other peaks are observed. The separation between the two peaks matches the valence band spin-splitting. Thus people attribute these two peaks to the excitons from the two spin-split bands and name them as A and B exciton peak respectively. The excitons can be excited resonantly, i.e., generating excitons using excitation energy close to the exciton emission energy even though the bandgap is much larger. The experimental estimation of the bandgap (lower bound) in WS_2 and WSe_2 is 2.91 eV and 2.53 eV respectively [27].

3.3.1 Dark Exciton in TMDs

Besides being classified by their radius and binding energy, excitons can also be classified by whether the electron and hole can radiatively recombine or not and they are named bright and dark excitons respectively. The reason why some excitons are dark is that radiative recombination would violate either momentum or spin conservation. For example, suppose there is an exciton with the electron and hole having parallel spin directions. This exciton carries a net spin. However, a photon does not carry spin. The conservation of spin prohibits the radiative recombination.

In most materials, PL intensity increases with decreasing temperature. Part of the reason is that at higher temperatures, the carriers have higher kinetic energy and are more likely to be scattered to non-radiative recombination centers or out of the light cone. However, in WSe_2 and WS_2, the PL intensity decreases with decreasing

the temperature, which is due to the transition from bright excitons to dark excitons [28].

Around the K and K′ points, the valence band mainly arises from the $d_{x^2-y^2}$ and d_{xy} orbitals of the transition metal element which result in hundreds of meV spin splitting. For the conduction band, in a simple band structure, it is formed by d_{z^2} and no spin splitting is expected [17]. However, taking into account the strongly coupled chalcogen orbitals and higher-order coupling, the conduction band also has a spin splitting. Depending on the sign of the correction terms, the spin splitting can either have the same or opposite sign to that of the valence band. In tungsten-based TMDs, the lower conduction band has opposite spin orientation to the upper valence band. Whereas in molybdenum-based TMDs, the spin orientation of the lower conduction band and the upper valence band are the same. At thermal equilibrium without considering the interactions between the electrons, the electron population in the upper and lower conduction band can be described by the Boltzmann distribution:

$$\frac{N_{upper}}{N_{upper}+N_{lower}} = \frac{e^{-\Delta/k_BT}}{1+e^{-\Delta/k_BT}} \tag{3.1}$$

where Δ is the spin splitting between the upper and lower conduction band. Following Eq (3.1), as the temperature decreases, more electrons relax to the lower conduction band. On the other hand, in tungsten based TMDs, the bright excitons are formed by the upper conduction band electrons and the upper valence band holes. This relaxation process makes the bright excitons dark. Besides intra-valley spin flipping, inter-valley scattering can also lead to dark excitons, in which radiative recombination violates the conservation of momentum.

CHAPTER IV

Experimental Methods to Measure the Spin Polarization

4.1 Faraday and Kerr Effect

In 1845, Faraday found that when linearly polarized light passes through a material in a longitudinal magnetic field, i.e. the magnetic field is along the optical path, the polarization direction rotates an angle [29]. The magnitude of the rotation angle θ is proportional to both the magnetic field B and the path length d which the light travels in the material:

$$\theta = \nu B d \tag{4.1}$$

The proportionality factor ν is called the Verdet constant for that material, and it depends on several factors such as the wavelength and temperature. Looking at Eq (4.1), it seems that an external magnetic field is essential to have the Faraday effect. However, it turns out that the role of the magnetic field is to make the material magnetized. In other words, as long as the material is magnetized, the interaction of the light and the magnetized material results in Faraday rotation even without the presence of a magnetic field. Magnetization is a macroscopic description of spin

polarization. Therefore Faraday rotation angle can be rewritten in terms of the spin polarization:

$$\theta = \sigma_F S_z d \tag{4.2}$$

where $S_z = \frac{n_\uparrow - n_\downarrow}{n_\uparrow + n_\downarrow}$ is the spin polarization and the proportionality factor σ_F is called Faraday cross section. Eq (4.2) provides us with a way to measure spin polarization using light, i.e. by measuring the Faraday rotation angle, one can determine the spin polarization .

The mechanisms behind Faraday rotation can be understood through the concept of circular birefringence [30]. The right circularly polarized light (RCP) and the left circularly polarized light (LCP) experience different refractive indices when traveling through the material. In the context of Faraday rotation, the circular birefringence arises from the spin-dependent optical selection rules. An unequal population of up and down spins in the conduction band gives rise to a shift in the absorption curves for the LCP and RCP[1] (Figure (4.1) (a)). Through the Kramers-Kronig relation [31], this translates to a shift in refractive indices (Figure (4.1) (b)). As we will see later, the difference of the refractive indices gives rise to a phase difference between the RCP and LCP. The phase difference causes a rotation of the linearly polarized light (Faraday rotation).

In general, linearly polarized light along the x-axis can be decomposed into RCP and LCP using the Jones matrix formalism [32]:

[1] In this simulation, we assume the absorption curve follows $\sqrt{E - Eg}$ for $E \geq Eg$ and $e^{((E-Eg)/W)}$ for $E < Eg$. When the photon energy is higher than the band gap, the absorption follows the density of states of 3D solid. When the photon energy is lower than the band gap, Urbach tail is used to capture the localized states below the band gap.

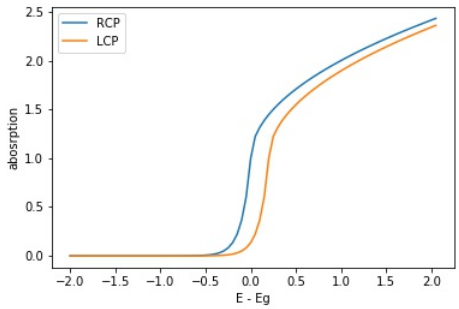

(a) Absorption curves for RCP and LCP in a spin polarized material.

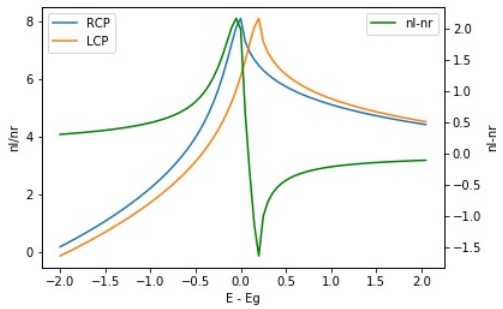

(b) Indices of refraction for RCP and LCP (left axis) and the difference between the two (right axis) in a spin polarized material.

Figure 4.1: The shift of absorption coefficients and indices of refraction in a spin polarized material.

$$E = e^{i(kz-wt)} \begin{pmatrix} 1 \\ 0 \end{pmatrix} = \frac{e^{i(kz-wt)}}{2} \begin{pmatrix} 1 \\ i \end{pmatrix} + \frac{e^{i(kz-wt)}}{2} \begin{pmatrix} 1 \\ -i \end{pmatrix} \tag{4.3}$$

Let n_r and n_l be the refractive index of the RCP and LCP, and the sample length is d, when the light transmits through the sample, it becomes:

$$E' = \frac{e^{i(n_r kd-wt)}}{2} \begin{pmatrix} 1 \\ i \end{pmatrix} + \frac{e^{i(n_l kd-wt)}}{2} \begin{pmatrix} 1 \\ -i \end{pmatrix} \tag{4.4}$$

Let $\phi = \frac{1}{2}(n_r kd + n_l kd)$ and $\theta = \frac{1}{2}(n_r kd - n_l kd)$, equation (4.4) can be written as:

$$E' = e^{i(\phi-wt)}(\frac{e^{i\theta}}{2} \begin{pmatrix} 1 \\ i \end{pmatrix} + \frac{e^{-i\theta}}{2} \begin{pmatrix} 1 \\ -i \end{pmatrix}) = e^{i(\phi-wt)} \begin{pmatrix} \cos(\theta) \\ -\sin(\theta) \end{pmatrix} \tag{4.5}$$

Eq (4.5) shows that the linearly polarized light rotates an angle θ because of circular birefringence. The rotation angle θ is proportional to $n_r - n_l$. Therefore the Faraday rotation angle follows the same energy dependence as $n_r - n_l$. The Faraday rotation angle changes sign when the photon energy crosses the band gap. As shown in Fig (4.1)(b), two photon energies maximize the Faraday rotation angle. One is

below the bandgap, and the other is above the bandgap. In most of our experiments, the photon energy is tuned such that it maximizes the Faraday rotation angle.

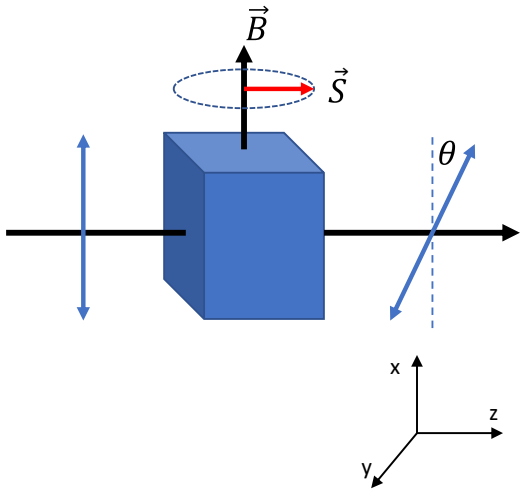

Figure 4.2: Spin polarization $\vec{S}$ measured by Faraday rotation. A transverse magnetic field can be applied to measure the g-factor of the carriers.

Figure (4.2) shows the idea of measuring spin polarization $\vec{S}$ using Faraday rotation. A transverse magnetic field $\vec{B}$ can be applied, along which $\vec{S}$ precesses. The Larmor precession frequency for electrons is:

$$\omega = \frac{g\mu_B|\vec{B}|}{\hbar} \tag{4.6}$$

where $\mu_B = \frac{e\hbar}{2m_e}$ is the Bohr magneton and g is the effective g-factor of the material. Although the g-factor of a free electron is close to 2, the effective g-factor of electrons in a semiconductor deviates from 2. For example, the electron g-factor in GaAs is about -0.4. The reason for this deviation is that the internal magnetic field is not taken into account in Eq (4.6). The effect of the internal field is described by the effective g-factor.

The idea of Kerr Effect is very similar to Faraday effect except that the reflection is measured instead of the transmission. In general, Kerr rotation measurements have three different geometries: polar, longitudinal and transversal as shown in Fig-

ure (4.3). In polar geometry, the spin polarization is perpendicular to the reflection surface and parallel to the incident plane. The incident light is usually perpendicular to the reflection plane. In longitudinal geometry, the spin polarization is parallel to both the reflection plane and the incident plane. This requires the incident light not being normal to the reflection surface. In transversal geometry, the spin polarization is perpendicular to the incident plane and parallel to the surface. The incident light is normal to the reflection surface, and instead of polarization, reflectivity is measured.

The spin polarization studied in this thesis is perpendicular to the reflection plane. All the Kerr rotation measurements that appear in this thesis are done in polar geometry.

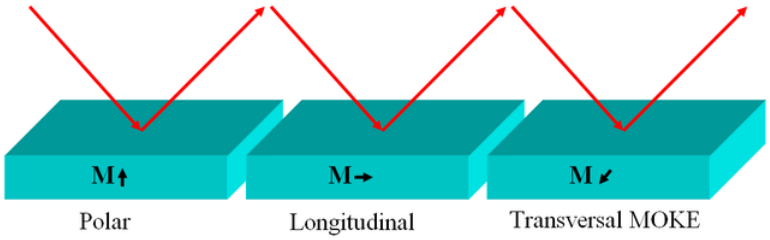

Figure 4.3: Three different Kerr rotation measurement geometries. M represents the magnetization direction and the red arrow represents the probe light. Source: Wikipedia

4.2 Time-Resolved Faraday/Kerr Rotation

Time-resolved Faraday/Kerr Rotation (TRFR/TRKR) is a powerful tool to study spin dynamics in semiconductors [33]. Spin polarization is created by a circularly polarized pump pulse, followed by a linearly polarized probe pulse that measures the spin polarization via Faraday/Kerr rotation. By changing the time delay Δt between the pump and probe, the spin dynamics at different time can be sampled. The changing of delay time is realized by changing the relative optical length between the pump and probe optical path. The schematic TRFR setup is shown in Figure (4.4).

The pump and probe are created by splitting the output of the laser into two

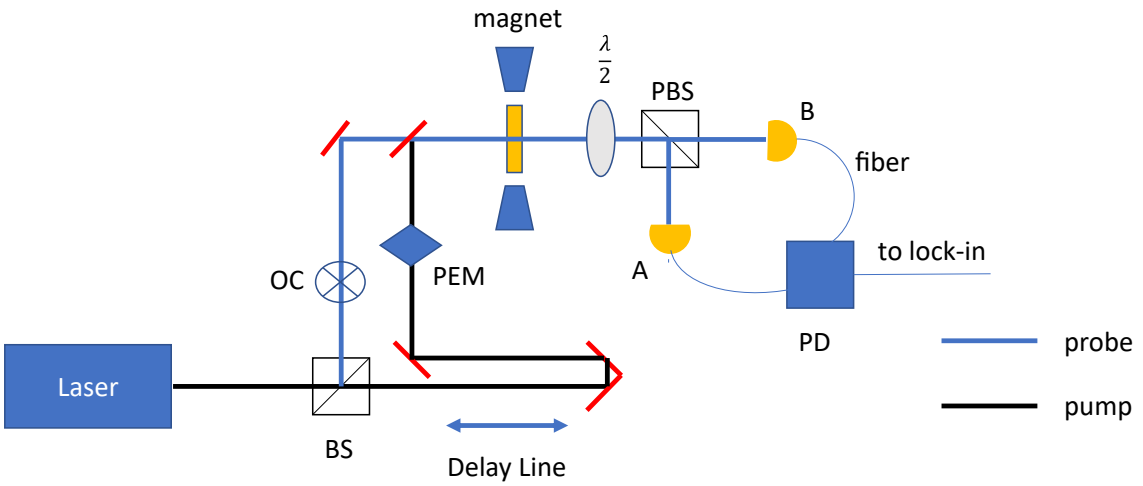

Figure 4.4: Time-resolved Faraday rotation setup. The output of the laser is split into pump and probe by a beam splitter (BS). The probe is modulated by an optical chopper (OC) and the pump is modulated by a PEM. After the sample, the probe is split by a polarization beam splitter (PBS) and sent to the two arms of the photodiode bridge (PD).

paths. The pump pulse is sent to an optical delay line so that the delay time between the pump and probe can be changed. In our lab, the laser source is a Mira 900 with a 76 MHz repetition rate, i.e., the repetition time period is 13.1 ns. This number sets the upper bound of the delay time we can use in experiments. Besides this constraint, the physical length of the delay line is another constraint on the delay time range. Knowing that light travels approximately 0.3 meters per nanosecond, one can roughly estimate the delay range. For example, a 0.9 meters long delay line corresponds to 6 ns delay range (you need to add a factor of 2 because it is a double path).

Although the total delay range is fixed by the length of the delay line, one has the freedom to choose the start and end point of the delay time range. For example, if the total delay range is 6 ns (determined by the physical length of the delay line), one can have the delay range, for example, from -1 ns to 5 ns or 2 ns to 8 ns. The negative delay time means the probe pulse arrives earlier than the pump pulse. Since we have a pulse train, the probe is detecting the spin polarization generated by the previous pump pulse. Therefore, -1 ns delay is effectively 12.1 ns delay. -1 ns to 5 ns

delay range is effectively 0 ns to 5ns and 12.1 ns to 13.1 ns. In practice, one usually wants to include the zero delay point in the delay range.

After passing the delay line, the pump pulse is sent to a photo-elastic modulator (PEM). A PEM is similar to a wave plate, except that the retardance between the fast and slow axis oscillates at a particular frequency f (50 kHz in our case). The maximum retardance of the PEM is set to be $\frac{\pi}{2}$ (quarter-wave retardance), and the fast and slow axis of the PEM is set to have an angle of $\frac{\pi}{4}$ with the incident pump light. Therefore, the pump light is modulated between RCP and LCP at frequency f. The PEM plays two roles here: 1. it changes the pump pulse from linearly polarized to circularly polarized. 2. it modulates the pump beam which enables us to use a lock-in amplifier to increase the signal to noise ratio (SNR) as we will see later.

After generated by the pump pulse, the spin polarization amplitude decreases because of spin relaxation. Phenomenologically, this relaxation can be described by a spin lifetime τ:

$$\theta(\Delta t) = A\exp(-\frac{\Delta t}{\tau}) \tag{4.7}$$

where A is the initial rotation amplitude and Δt is the time difference between the pump and probe. When a transverse magnetic field is applied, the spin polarization starts to precess. The rotation angle is described by:

$$\theta(\Delta t, B) = A\exp(-\frac{\Delta t}{\tau})\cos(\frac{g\mu_B B}{\hbar}\Delta t) \tag{4.8}$$

This is an exponential decaying cosine. Figure (4.5) shows the TRFR signal of bulk GaAs.

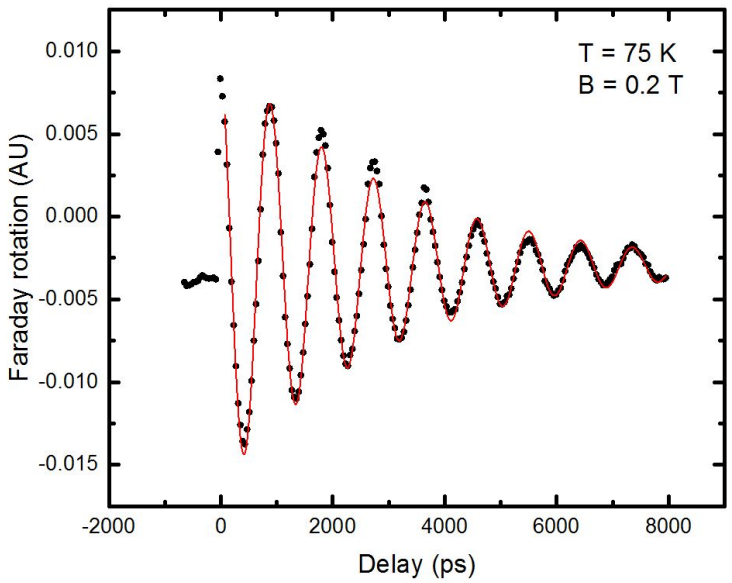

Figure 4.5: TRFR results on bulk GaAs. Experiment parameters: T = 75 K, B = 0.2 T, λ = 843 nm. Fitting parameters: lifetime = 3 ns, g = 0.39

4.3 Resonant Spin Amplification

In TRFR/TRKR measurements, the transverse magnetic field is fixed and the time difference between the pump and probe varies (i.e. the measurement is done in the time domain). One can conduct the experiments in a different way: varying the magnetic field at a fixed delay time. This measurement technique is called resonant spin amplification (RSA) [34]. RSA is often used when the spin lifetime is longer than the laser repetition period. At some particular magnetic fields, the spin polarization generated by different pump pulses interfere constructively. Since the Larmor precession frequency is proportional to the magnetic field, changing the magnetic field is equivalent to changing the precession frequency. Thus, RSA can be viewed as measuring the spin polarization in the frequency domain.

When the spin lifetime τ is comparable to the laser repetition period t_{rep}, the previous pulses also contribute to the rotation. Taking into account the effect from the previous pulses, Eq (4.8) should be rewritten as:

$$\theta(\Delta t, B) = \sum_{i=0}^{\infty} A \exp(-\frac{\Delta t + i * t_{rep}}{\tau}) \cos(\frac{g\mu_B B}{\hbar}(\Delta t + i * t_{rep})) \tag{4.9}$$

In reality, we do not need to sum to infinity because the amplitude of each term in Eq (4.9) decreases exponentially. For example, in the case of t_{rep} = 13 ns and τ = 20 ns, summing over 5 terms is already good enough.

Figure (4.6) shows a typical RSA scan of bulk GaAs. It has several spikes distributed evenly. The separation between the spikes is determined by t_{rep}. The width of the spikes is inversely proportional to the spin lifetime τ.

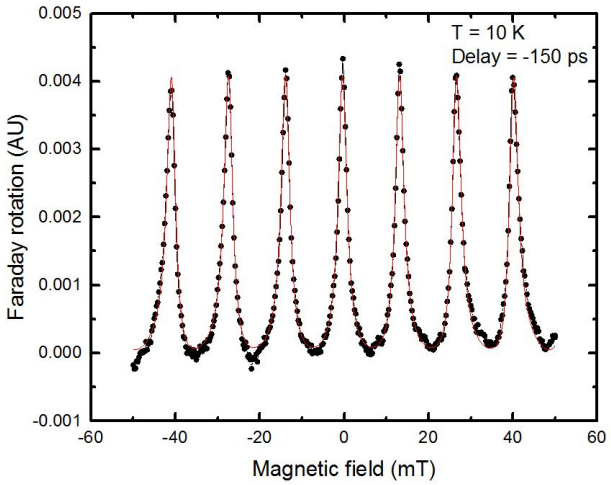

Figure 4.6: RSA results on bulk GaAs at 10 K and -150 ps delay. The red curve is the fit using the first 4 terms in equation (4.9). The lifetime and g-factor extracted from the fitting are 22 ns and 0.40 respectively.

The origin of the spikes comes from the constructive interference between the spin polarization generated by the current and previous pulses, i.e., when the current pump pulse reaches the sample, the spin polarization created by previous pulses precessed $2\pi j$ ($j = 0, 1, 2 \cdots$) which requires the magnetic field to satisfy the following condition:

$$\begin{aligned} &\frac{g\mu_B \hat{B}}{\hbar} t_{rep} = 2\pi j \qquad \text{(j=0,1,2,3}\cdots\text{)} \\ &\Rightarrow \hat{B} = \frac{2\pi\hbar}{g\mu_B t_{rep}} j \end{aligned} \tag{4.10}$$

Eq (4.10) states that the separations between the spikes are the same and are only determined by the laser repetition time t_{rep}. The longer the lifetime τ, the more terms will be included in the summation in Eq (4.9), which results in stronger interference and narrower spike width. In Figure (4.7), we show some RSA simulation results using different delay times and lifetimes (consider three previous pulses).

Generally speaking, there are two periods in a RSA scan. One is determined by the laser repetition time t_{rep}. From Eq (4.10), it is easy to know this period is $B_{t_{rep}} = \frac{2\pi\hbar}{g\mu_B t_{rep}}$. Another period is determined by the delay time Δt: $B_{\Delta t} = \frac{2\pi\hbar}{g\mu_B \Delta t}$.

Figure (4.7) shows how the RSA signal looks like at different delay times with t_{rep} = 13 ns (a, b, c) and t_{rep} = 5 ns (d). Figure (4.7) (a) shows the RSA signal with a Δt = 50 ps, which is much shorter than t_{rep} (thus $B_{\Delta t} \gg B_{t_{rep}}$). The spikes are on a relatively flat background. We need to increase the magnetic field scan range to observe the period of $B_{\Delta t}$. Figure (4.7)(b) shows the RSA signal with a Δt = 2 ns. In this case, $B_{\Delta t}$ is not too large, several oscillations can be seen between -0.2 T to 0.2 T. Figure (4.7) (c) shows the RSA signal with a Δt = -150 ps (12.85 ns). In this case, since Δt is very close to t_{rep}, the two periods are very close. It is hard to distinguish the period of $B_{\Delta t}$ and $B_{t_{rep}}$. Figure (4.7) (d) shows how the RSA looks like when the lifetime is short relative to the t_{rep}. Note that the width of the spikes are much larger and the peak height are much lower both indicating short lifetime. In real experiments, the heights of these small peaks are comparable to the noise level and hard to observe.

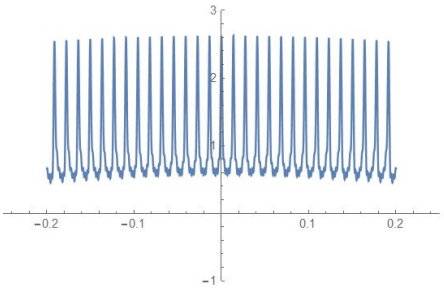

(a) Delay time = 50 ps, lifetime = 30 ns

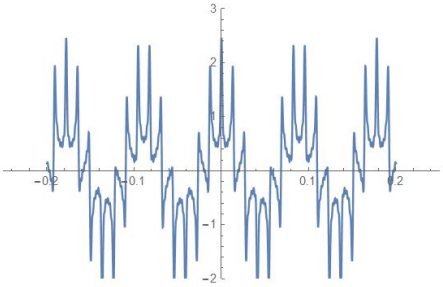

(b) Delay time = 2 ns, lifetime = 30 ns

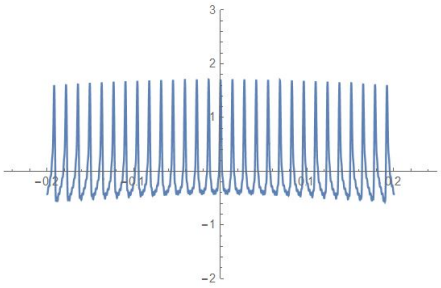

(c) Delay time = -150 ps, lifetime = 30 ns

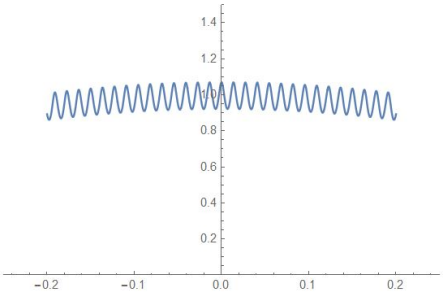

(d) Delay time = 50 ps, lifetime = 5 ns

Figure 4.7: Simulation of RSA. Horizontal axis: magnetic field (T), vertical axis: Faraday/Kerr rotation signal (arbitrary unit). The simulation take into account 5 previous pulses with t_{rep} = 13 ns and g = 0.4.

4.4 Spatially-Resolved Faraday/Kerr Measurements

In TRFR/TRKR and RSA, the spatial position of the pump and probe spots are fixed; the varying experimental parameters are the delay time and external magnetic field. In some cases, we are more interested in the spatial profile of the spin packet or the spin diffusion constant. Spatially-resolved Faraday/Kerr measurements can be done where the pump is scanned over the probe spatially, and the Faraday/Kerr rotation signal is measured.

Suppose the pump pulse has a Gaussian shape (intensity) whose standard deviation is σ_0. Therefore, the spatial distribution of the pump generated spin density is also a Gaussian at t = 0 (in polar coordinate system):

$$f(r,t)|_{t=0} = \frac{S_0}{\sqrt{2\pi\sigma_0^2}} \exp(-\frac{r^2}{2\sigma_0^2}) \tag{4.11}$$

where S_0 is the total number of spins generated by the pump. For t > 0, the spins start to diffuse following the diffusion equation:

$$\frac{\partial f}{\partial t} = D\frac{1}{r}\frac{\partial}{\partial r}(r\frac{\partial f}{\partial r}) - \frac{f}{\tau} \tag{4.12}$$

where D is the diffusion constant and τ is the spin relaxation time. The solution of Eq (4.12) with Eq (4.11) as the initial condition is:

$$f(r,t) = \frac{S_0}{\sqrt{2\pi(\sigma_0^2 + 2Dt)}} \exp(\frac{-r^2}{2(\sigma_0^2 + 2Dt)}) \exp(\frac{-t}{\tau}) \tag{4.13}$$

Eq (4.13) described how the spin spatial profile changes with time. A probe is used to measure this spin profile. Suppose the probe is also a Gaussian beam with σ_1 as its standard deviation:

$$P(r) = \frac{A}{\sqrt{2\pi\sigma_1^2}} \exp(-\frac{r^2}{2\sigma_1^2}) \tag{4.14}$$

Scanning the probe over the pump is equivalent to doing convolution between the pump and probe.[2] Without losing generality, we assume the scanning is along the x-axis. To make the math easier, we switch back to the Cartesian coordinate system by substituting r^2 with $x^2 + y^2$:

[2]In actual experiments, the probe is fixed and the pump scans over the probe due to technical reasons. Since scanning the pump or probe is equivalent, for simplicity, we assume scanning the probe in this derivation.

$$
\begin{aligned}
f(x,y,t) \circledast P(x,y) =& \frac{S_0 exp(-\frac{t}{\tau})}{\sqrt{2\pi(\sigma_0^2+2Dt)}} exp(-\frac{y^2}{2(\sigma_0^2+2Dt)}) \frac{A}{\sqrt{2\pi\sigma_1^2}} exp(-\frac{y^2}{2\sigma_1^2}) \\
& \int_{-\infty}^{+\infty} ds\, exp(-\frac{x^2}{2(\sigma_0^2+2Dt)}) exp(-\frac{(s-x)^2}{2\sigma_1^2}) \\
=& \frac{S_0 exp(-\frac{t}{\tau})}{\sqrt{2\pi(\sigma_0^2+2Dt)}} exp(-\frac{y^2}{2(\sigma_0^2+2Dt)}) \frac{A}{\sqrt{2\pi\sigma_1^2}} exp(-\frac{y^2}{2\sigma_1^2}) \\
& \frac{1}{\sqrt{2\pi(\sigma_0^2+\sigma_1^2+2Dt)}} exp(\frac{x^2}{2(\sigma_0^2+\sigma_1^2+2Dt)})
\end{aligned}
\tag{4.15}
$$

where $\circledast$ represents convolution operation. The above derivation used the fact that the convolution of two Gaussians $N(\mu_1, \sigma_1)$, $N(\mu_2, \sigma_2)$ is still a Gaussian $N(\mu_3, \sigma_3)$, where $\mu_3 = \mu_1 + \mu_2$ and $\sigma_3^2 = \sigma_1^2 + \sigma_2^2$ [35]. Since the scanning is done along the x-axis, the information along y-axis is integrated automatically (no spatial information along y-axis can be retrieved). Therefore, we need to integrate along the y-axis in equation (4.15) to get our result:

$$
\begin{aligned}
Signal(x,t) &= \int_{-\infty}^{+\infty} dy\, f(x,y,t) \circledast P(x,y) \\
&= \frac{S_0 A}{\sqrt{2\pi(\sigma_0^2+\sigma_1^2+2Dt)}} exp(-\frac{x^2}{2(\sigma_0^2+\sigma_1^2+2Dt)}) exp(-\frac{t}{\tau}) \\
&= \frac{B(t)}{\sqrt{2\pi\sigma_3^2}} exp(-\frac{x^2}{2\sigma_3^2})
\end{aligned}
\tag{4.16}
$$

where $B(t) = S_0 A exp(-\frac{t}{\tau})$ and $\sigma_3^2 = \sigma_0^2 + \sigma_1^2 + 2Dt$. Eq (4.16) states that the shape of the spatial resolved Faraday/Kerr rotation signal is a Gaussian. At a fixed time delay t, the area under the curve gives $B(t)$. Spin relaxation time τ can be extracted if B(t) is measured at several different delay times. The standard deviation of the signal σ_3 has a linear relation with the delay time t whose slope gives the spin diffusion constant.

4.5 Faraday/Kerr Rotation Detection

The easiest way to measure the rotation of linearly polarized light is using a polarizer and a photodetector. First, rotate the polarizer such that the light intensity on the detector is maximized. We denote this intensity as I_0. At this angle, the linearly polarized light aligns with the polarizer. Assume the polarization direction rotates an angle θ, part of the light is blocked by the polarizer and the intensity on the detector drops to I. The relationship between I and I_0 is as follows:

$$I = I_0 \cos^2(\theta) \tag{4.17}$$

By calculating the ratio between I and I_0, we can get the rotation angle θ. However, the resolution and accuracy of this simple method are low. Also it suffers from laser power fluctuation. Usually, the Faraday/Kerr rotation angle from the semiconductors is on the scale of microradians, which is beyond the resolution of this simple method. An alternative is using a polarization beam splitter, a half wave plate, and a photodiode bridge. The photodiode bridge converts the light intensity to a voltage. It has two input channels A and B, and three output channels A, B, and A-B. A schematic is shown in Figure (4.8) (a).

First, the linearly polarized light is adjusted to have $\frac{\pi}{4}$ angle relative to the optical axes (horizontal: x, vertical: y) of the polarization beam splitter. This adjustment can be done by rotating the half wave plate. The polarization beam splitter spatially separates the x and y polarization components. Each component is sent to the A and B channel of the photodiode bridge respectively. Since the light has equal amount x and y component, the output A-B is zero.

Suppose the pump is turned on and the sample is spin-polarized. The probe light experiences a rotation θ, and the intensities at channel A and channel B become:

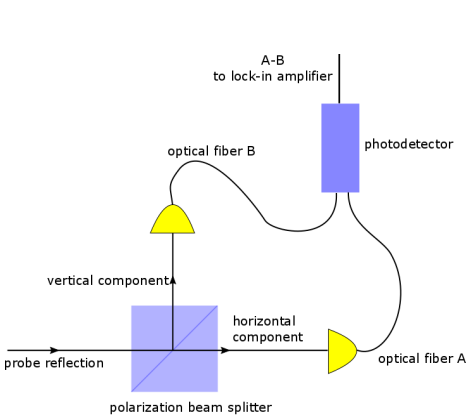

(a) Schematic of Faraday/Kerr rotation detection setup.

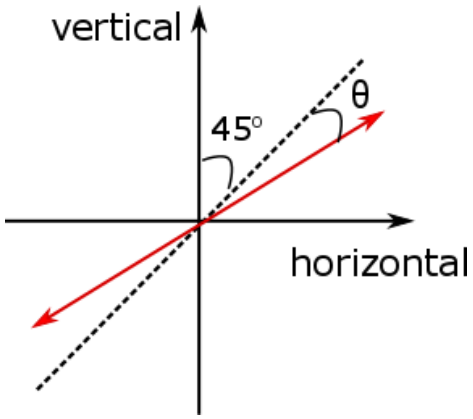

(b) The probe polarization direction rotates an angle θ which causes an imbalance between the vertical and horizontal components.

Figure 4.8: Faraday/Kerr rotation detection setup.

$$
\begin{aligned}
I_x &= I_0 \cos^2(\frac{\pi}{4} - \theta) \\
I_y &= I_0 \sin^2(\frac{\pi}{4} - \theta)
\end{aligned}
\tag{4.18}
$$

The difference of channel A and channel B is:

$$
\begin{aligned}
I_x - I_y &= I_0(\cos^2(\frac{\pi}{4} - \theta) - \sin^2(\frac{\pi}{4} - \theta)) \\
&= I_0(\frac{1 + cos(\frac{\pi}{2} - 2\theta)}{2} - \frac{1 - \cos(\frac{\pi}{2} - 2\theta)}{2}) \\
&= I_0 \cos(\frac{\pi}{2} - 2\theta) \\
&= I_0 \sin(2\theta) \\
&\approx I_0 2\theta
\end{aligned}
\tag{4.19}
$$

The rotation angle θ can be written as:

$$
\theta = \frac{1}{2}\frac{I_x - I_y}{I_0} = \frac{1}{2}\frac{I_x - I_y}{I_x + I_y} \tag{4.20}
$$

Eq (4.20) shows that the rotation angle can be measured by calculating the ratio of the difference and sum of channel A and channel B. In reality, measuring the absolute value of θ is not very straightforward. One needs to figure out the gain settings of the photodiode bridge and the lock-in amplifiers. Fortunately, in most cases, we do not need to know the absolute value of the rotation angle. Knowing the rotation angle up to a factor is enough to extract the lifetime and g-factor. Besides higher detection resolution, the photodiode bridge measurement technique is also robust to laser power fluctuations because the fluctuation on the two channels cancels when we consider the intensity difference of the two channels $I_x - I_y$ (However, the fluctuation still contributes to the total intensity $I_x + I_y$).

4.6 Cascaded Lock-in Amplifier Measurement Technique

The lock-in amplifier measurement technique is a powerful tool to measure small signals (compared to the noise level). It utilizes the orthonormal property of the Fourier components. Roughly speaking, what the lock-in does is multiply the reference frequency with the input signal. The resulting signal is then sent to a low pass filter to remove the high-frequency components. Intuitively, one can think the lock-in amplifier increases the signal to noise ratio (SNR) by narrowing down the detection region in the frequency domain as shown in Figure (4.9). Since the white noise has a uniform distribution in the frequency domain, most of it is filtered out.

Here we use a simple example to show how the lock-in removes the noise. Suppose the input signal consists of two components: one is at frequency f_0, the other is at frequency f' ($\mathrm{f}_0 \neq \mathrm{f}'$). We want to measure the amplitude of the signal at f_0. The component at frequency f' is what we want to remove. The reference frequency of the lock-in amplifier is set at f_0. The input signal can be written as:

$$A\cos(2\pi f_0 t) + B\cos(2\pi f' t) \tag{4.21}$$

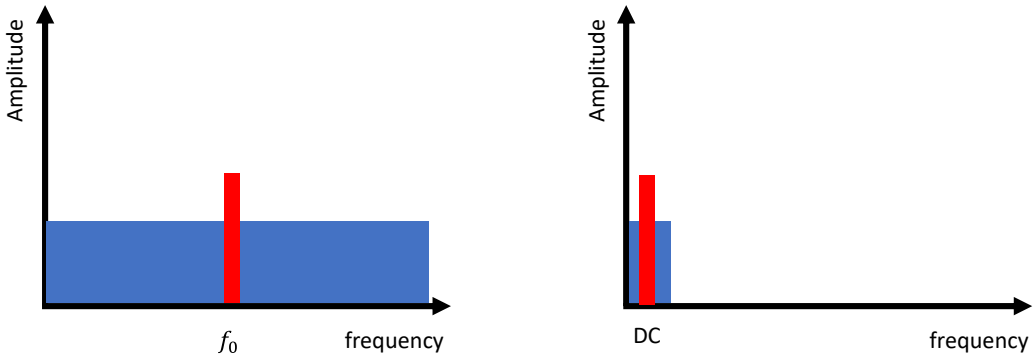

(a) The modulated signal at f_0 (red) and the white noise (blue) in the frequency domain.

(b) Signal is moved to DC and most of the white noise is filtered out by the low-pass filter.

Figure 4.9: Demonstration of how the lock-in amplifier increases signal to noise ratio. The signal is represented by the red rectangle and the white noise is represented by the blue rectangle. Here we assume the white noise is distributed uniformly in the frequency domain. The area ratio between the red and blue rectangle represents the SNR. (a) is the input signal to the lock-in amplifier. (b) is the output of the lock-in amplifier.

After multiplying the reference frequency f_0, the input signal becomes:

$$\begin{aligned} &(A\cos(2\pi f_0 t) + B\cos(2\pi f' t))cos(2\pi f_0 t) \\ =&A\cos^2(2\pi f_0 t) + B\cos(2\pi f' t)cos(2\pi f_0 t) \\ =&\frac{A}{2} + \frac{A}{2}\cos(4\pi f_0 t) + \frac{B}{2}\cos(2\pi(f' - f_0)t) + \frac{B}{2}\cos(2\pi(f' + f_0)t) \end{aligned} \tag{4.22}$$

Note in Eq (4.22) only the first term is DC which can pass the low pass filter (for simplicity we assume the low pass filter's cutoff frequency is very close to 0). The lock-in amplifier's output is $\frac{A}{2}$. The lock-in amplifier removes the noise at frequency f' at the cost of decreasing the signal by half.

In TRFR/TRKR measurements, since the pump is modulated at the PEM frequency f_1, the spin polarization generated by the pump is also at f_1. If the probe light is not modulated, the Faraday/Kerr rotation is at frequency f_1. In some cases, the pump and probe might be spatially separated, and only the probe light can reach the

photodiode bridge. It is okay to lock to frequency f_1 and measure the Faraday/Kerr rotation angle with one lock-in. In other cases, the pump and probe are hard to separate spatially, and the pump scatter can overwhelm the probe signal if we only use one lock-in. An alternative is modulating both the pump and probe and using two lock-in amplifiers to lock to the pump and probe frequency respectively. The output of the first lock-in amplifier is sent to the second lock-in amplifier, thus the name cascaded lock-in technique. This technique helps to remove the pump scatter and improve the SNR.

Suppose the pump light and probe light are modulated at frequency f_1 and f_2 respectively (usually $f_1 \gg f_2$). The Kerr rotation signal is proportional to the multiplication of the pump and probe frequency. The total signal at the photodiode bridge can be written as (Figure (4.10)(a)):

$$\begin{aligned} Signal_0 &= A\cos(2\pi f_1 t)\cos(2\pi f_2 t) + B\cos(2\pi f_1 t) \\ &= \frac{A}{2}\cos(2\pi(f_1+f_2)t) + \frac{A}{2}\cos(2\pi(f_1-f_2)t) + B\cos(2\pi f_1 t) \end{aligned} \tag{4.23}$$

where A is the amplitude of the rotation signal we care about and B is the amplitude of pump scatter we want to remove. For simplicity, we ignore the white noise term (which is an infinite series). The total signal is sent to the first lock-in amplifier which locks to frequency f_1. After the first signal multiplier (multiply $Signal_0$ with $\cos(2\pi f_1 t)$), the signal becomes (Figure (4.10) (b)):

$$\begin{aligned} Signal_1 = &\frac{A}{4}\cos(2\pi(2f_1+f_2)t) + \frac{A}{2}\cos(2\pi f_2 t) \\ &+ \frac{A}{4}\cos(2\pi(2f_1-f_2)t) + \frac{B}{2}\cos(2\pi * 2f_1 t) + \frac{B}{2} \end{aligned} \tag{4.24}$$

The signal now contains five different frequencies: DC, f_2, $2f_1$ - f_2, $2f_1$, $2f_1$ + f_2. Since $f_1 \gg f_2$, $2f_1$ - f_2 and 2_1 + f_2 are very close to $2f_1$. The signal is then filtered by a

low-pass filter. The cutoff frequency can be changed by adjusting the time constant. Our goal is to remove components from pump scatter, i.e., those components that are related to B. Thus the cutoff frequency should be chosen such that only DC, and f_2 components can pass it. The signal after the low-pass filter is (Figure (4.10) (b)):

$$Signal_2 = \frac{A}{2}\cos(2\pi f_2 t) + \frac{B}{2} \tag{4.25}$$

After the first lock-in amplifier, both the Faraday/Kerr rotation signal and the pump scatter are cut in half. But the good thing is that the Faraday/Kerr rotation signal is at frequency f_2, and the pump scatter is at DC. We can use the second lock-in to remove the pump scatter easily by setting the second lock-in lock to frequency f_2. After multiplying with the reference frequency f_2, the signal is (Figure (4.10) (c)):

$$Signal_3 = \frac{A}{4} + \frac{A}{4}\cos(2\pi * 2 f_2 t) + \frac{B}{2}\cos(2\pi f_2 t) \tag{4.26}$$

It has DC, f_2 and $2f_2$ component. The low-pass filter filters out the two AC components and the final signal contains only the Faraday/ Kerr rotation signal with an amplitude $\frac{A}{4}$. The pump scatter is totally removed with the cost that the Faraday/Kerr rotation signal decreased by a factor of 4.

The cutoff frequency can be adjusted by changing the time constant (TC) of the lock-in (The cutoff frequency is equal to TC^{-1}). The other thing we can tune is the low-pass filter's rolloff. The lock-in in our lab has four choices for the rolloff: 6 dB, 12 dB, 18 dB and 24 dB per Octave. One Octave means doubling the frequency. 6 dB per Octave can be interpreted as the signal amplitude decreases by a factor of 2 when the frequency doubles (relative to the cutoff frequency).

We should be careful when we choose the TC for the first lock-in amplifier. On the one hand, the cutoff frequency should be large enough to allow the Faraday rotation signal to pass the filter. On the other hand, the cutoff frequency should be small

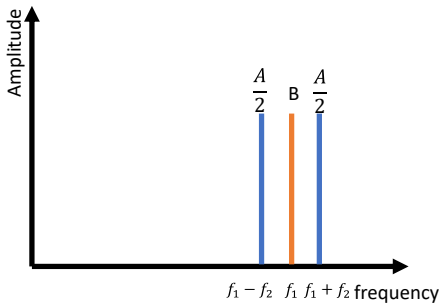

(a) Faraday/Kerr rotation signal with pump scatter (Eq (4.23)).

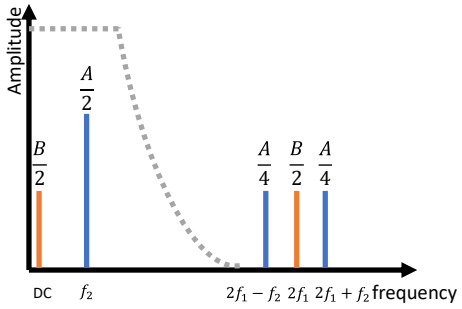

(b) Signal after multiplying reference frequency f_1 and the profile of the low-pass filter of the first lock-in (Eq (4.24), Eq (4.25)).

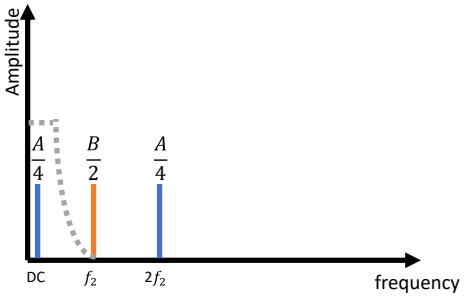

(c) Signal after multiplying reference frequency f_2 and the profile of the low pass filter of the second lock-in amplifier (Eq (4.26)).

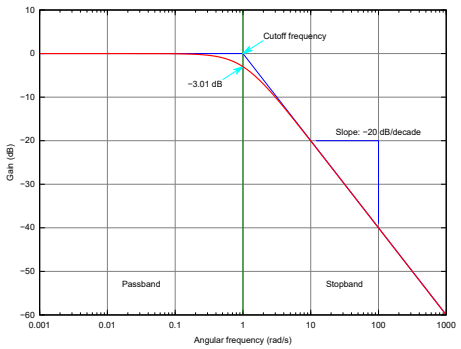

(d) The gain-magnitude frequency response of a first-order low-pass filter. The power rolloff is 20 dB per decade (6 dB per Octave). Source:Wikipedia

Figure 4.10: Illustration of cascaded lock-in technique and the frequency response of a typical low-pass filter.

enough so that the pump scatter can be filtered out. The dash line in Figure (4.10)(b) shows one possible low-pass filter choice. In practice, f_1 = 50 kHz and f_2 = 500 Hz. The TC is usually set at 160 μs (6.25 kHz cutoff frequency) with 6 dB/Octave rolloff, the pump scatter at $2f_1$ is decrease by 96 dB. If one wants to further filter out noise, higher rolloff settings can be used.

CHAPTER V

Long-lived Spin/Valley Polarization in Monolayer WSe_2

5.1 Photoluminescence of Monolayer WSe_2

As we discussed in Chapter IV, the amplitude of the Faraday/Kerr rotation signal highly depends on the excitation wavelength. In direct bandgap III-V semiconductors, the band-to-band transition has the strongest oscillator strength. Whereas in TMDs, the optical response is dominated by exciton states within the bandgap. The excitation energy should be tuned close to the difference between bandgap and exciton binding energy to maximize the Faraday/Kerr rotation. In both cases (band-to-band transition and exciton), PL emission spectra give useful information about the proper wavelength that maximize the Faraday/Kerr rotation signal.

Temperature-dependent PL measurements are done on two monolayer WSe_2 samples (WSe64-9 and WSe90-6-2). The results are shown in Figure (5.1) and Figure (5.2).

For sample WSe64-9, at room temperature (293 K), the PL emission peak centers at 1.65 eV. As the temperature decreases, the peak shifts to higher energy. A new peak at the low energy side starts to appear at 120 K and finally becomes the dominant peak below 50 K. Between 120 K and 50 K, both of the two peaks exist and the total

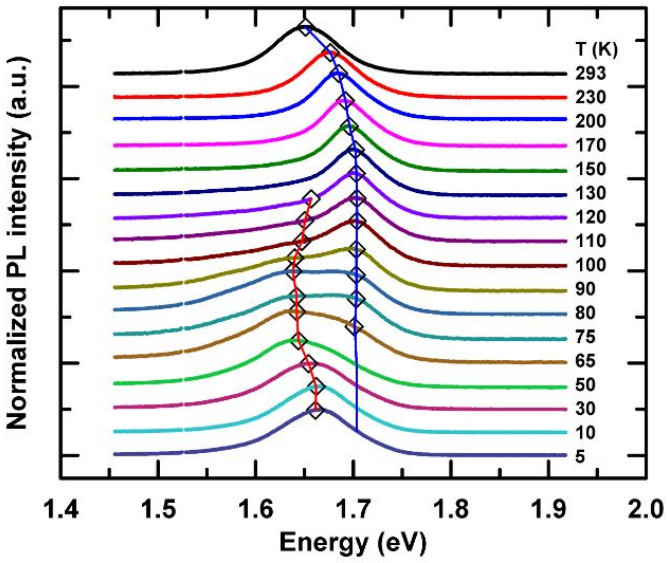

Figure 5.1: Normalized PL spectra versus photon energy at different temperatures on sample WSe64-9. All the spectra are measured with an excitation wavelength of 532 nm. The blue line is the fit using the temperature-dependent semiconductor band gap formula (Eq (5.1)). The red line is a guide to the eye for the localized exciton peak shift.

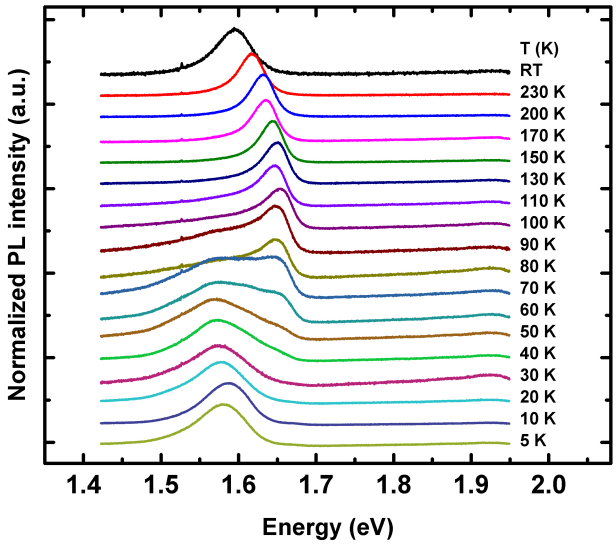

Figure 5.2: Normalized PL spectra versus photon energy at different temperatures on sample WSe90-6-2. The excitation wavelength is 532 nm. The spectra is very similar to WSe64-9 except the peaks are red-shifted.

PL emission is the superposition of the two. By fitting the PL emission using the sum of two Gaussians, the center and width of the two sub-peaks can be extracted. Figure (5.3), shows the fitting results at several different temperatures between 120 K and 65 K. The high and low energy peak are attributed to free excitons (FX) and localized excitons (LX) respectively. The possible origin of the LX peak could be disorder or defects in the sample. SiO_2/Si substrates usually display a large surface roughness of 4-8 Å, which can cause disorder and defects in the monolayer WSe_2 [36]. At low temperatures, the free excitons have less kinetic energy and are more likely to be trapped by defects and become localized excitons which explains the disappearance of the FX peak and the emergence of LX peak at low temperatures.

Sample WSe90-6-2 shows very similar photoluminescence spectra except the peaks are red-shifted. The red-shift could be due to the different growth conditions of sample growth process.

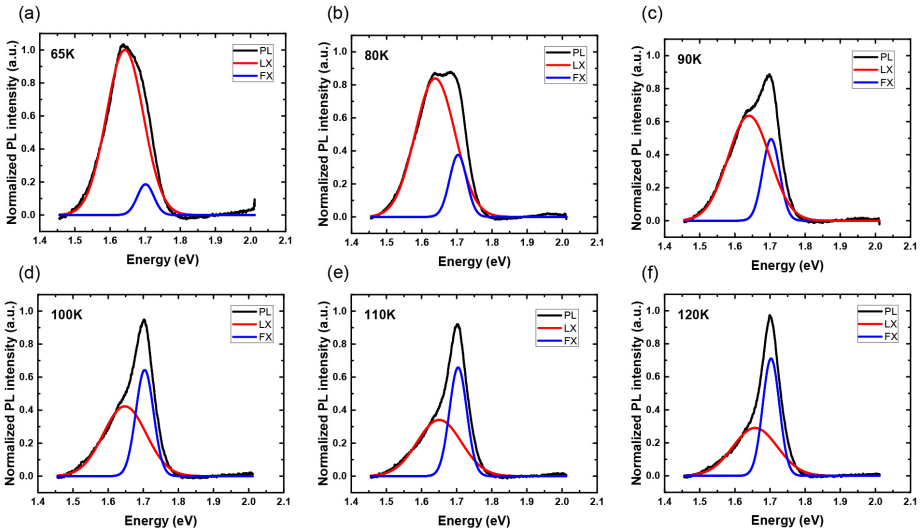

Figure 5.3: PL spectra at temperatures where both the free exciton peak and the localized exciton peak exist. The localized exciton peak (red line) and free exciton peak (blue line) are obtained by fitting the PL spectra using the sum of two Gaussians. The primary PL emission peak changes from the localized exciton peak to the free exciton peak with the increase of the temperature.

Interestingly, since the Coulomb interactions are strong in 2D TMDs, the FX emission energy is the difference between the bandgap and the exciton binding energy

(not the bandgap energy). However, the blue shift of the FX peak with decreasing the temperature matches pretty well with the temperature-dependent semiconductor bandgap formula[1] [37]:

$$E_g(T) = E_g(0) - S < \hbar w > [coth(\frac{< \hbar w >}{2k_B T} - 1)] \tag{5.1}$$

where $E_g(0)$ is the bandgap at 0 K, S is a dimensionless coupling constant and $< \hbar w >$ is an average phonon energy. The best fit gives $E_g(0) = 1.704$ eV, $S = 3.5$ and $< \hbar w >= 0.02$ eV.

In contrast, the LX peak has more complicated trends. It first shifts to lower energy (5 K - 65 K) then moves back to higher energy (65 K - 120 K) with increasing temperature. Similar behavior is observed in InGaN/GaN multiple quantum wells [38]. The possible explanation could be: between 5 K and 65 K the excitons can overcome local potential barriers and find lower defect states with increasing kinetic energy. Thus, the emission energy is decreasing with increasing temperature. However, between 65 K and 120 K, the photo-recombination time decreases and the electrons and holes recombine before reaching the lowest energy state causing the blue shift.

5.2 Time-Resolved Kerr Rotation Measurements of WSe_2

Time-resolved Kerr rotation measurements are performed to explore the spin/valley dynamics in monolayer WSe_2. Figure (5.4) shows the TRKR measurement results at 10 K with 726.5 nm pump and probe with the corresponding fit.

Since the laser source generates a train of pulses, the data points at negative delay times represent the Kerr rotation amplitude generated by the previous pulses. If the lifetime in the sample is much shorter than the laser repetition period, 13.1 ns in our

[1]This formula is a replacement of the Varshni equation: $E_g(T) = E_0 - \alpha T^2/(T + \beta)$.

case, the signal generated by the earlier pulses has already died out when the current probe arrives. Therefore, only the spin-unrelated background offset is measured at a negative delay. Ideally, this background offset should be zero. However, a lot of factors can make the background offset non-zero such as an unbalanced photodiode bridge, the offset from the lock-in amplifier etc..

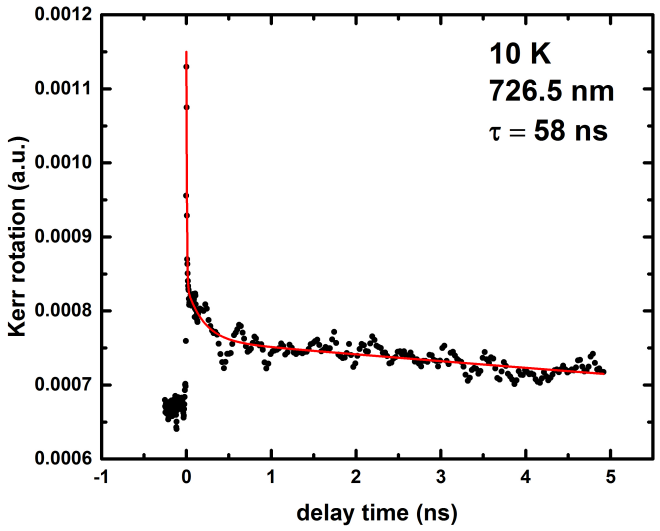

Figure 5.4: Time-resolved Kerr rotation measurement of monolayer WSe_2 at 10 K (sample WSe64-9). The black dots are data points and the red line is the fit using the sum of three exponential decays. The longest time scale extracted from the fit is 58 ns.

In Figure (5.4) the Kerr rotation amplitude is not around zero at the negative delay. There could be two possibilities. One is the background offset is large and the lifetime is about a few nanoseconds. The other is the lifetime is much longer than the laser repetition period, and spin signal persists beyond one laser repetition period. The TRKR measurement results alone can not distinguish between the two. However, spatially-resolved Kerr rotation measurements would give different results for these two cases. If the TRKR signal at negative delay is due to an offset, a spatially-resolved scan at the negative delay would only detect the offset. No Gaussian curve would be observed. On the other hand, if the signal is due to the residual polarization from

previous pulses, the spatially-resolved scan would give a Gaussian curve (Please refer to Chapter 4.4 for more details on spatially-resolved scans).

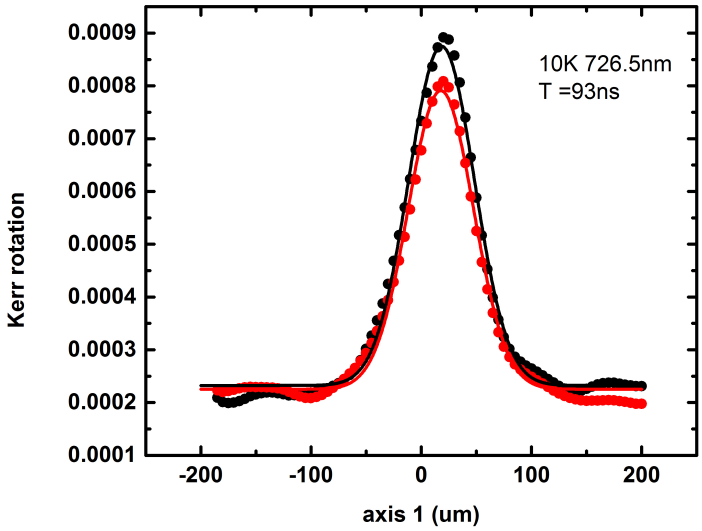

Figure 5.5: Spatial-resolved Kerr rotation measurements at delay time 1 ns (red) and -200 ps (black) on sample WSe64-9. The solid lines are fits with a Gaussian function.

Figure (5.5) shows the spatially-resolved scan at 1 ns and -200 ps (corresponding to 12.95 ns) at 10 K with 726.5 nm pump and probe. Surprisingly, the Gaussian height at -200 ps is very close to that at 1 ns. At negative delay, the Kerr rotation signal is still a Gaussian, which indicates a very long lifetime, which verifies that the large TRKR signal at negative delay is not a background offset.

To extract the slow decay time, we need to come up with a model to fit the data. There are roughly three decays in Figure (5.4): a fast decay (the first a few picoseconds after the excitation), an intermediate decay (the early hundreds of picoseconds) and a slow decay[2]. The most straightforward model that captures these features is the sum of three exponential decays:

$$A(t) = A_1 e^{-t/\tau_1} + A_2 e^{-t/\tau_2} + A_3 e^{-t/\tau_3} + A_0 \tag{5.2}$$

[2]At some temperatures and wavelength, the medium decay curve does not show up. The origin of the medium decay is still an open question. We will discuss this later in this chapter.

where τ_1, τ_2 and τ_3 capture the fast, intermediate and the slow decay respectively. A_1, A_2 and A_3 are the amplitudes of these three components. A_0 is the background offset which is not time or spin dependent. Since τ_3 and A_0 are correlated, the fit does not converge if both of them are free fitting parameters[3]. A_0 has to be determined first and fixed during the fitting process. Fortunately, A_0 can be extracted from the background offset in the spatially-resolved Kerr rotation scans. Since there are fluctuations between different runs, the mean of a few spatially-resolved scans (5-8 runs) is used. Knowing A_0, the fitting converges and the long lifetime τ_3 from TRKR is 58 ns (standard error = 5 ns).

τ_3 can be fit more accurately if the negative delay data is also taken into account[4]. As we mentioned before, $-t$ is effectively equivalent to $t_{rep} - t$. The fitting result with the negative delay data points are shown in Figure (5.6). τ_3 is 76 ns with smaller standard error (standard error = 2 ns). Fitting the data with negative delay points increases both the number of data points and the points span range, which gives less standard error of the fitting parameters. Without further notification, the TRKR data are fit with the negative delay data points in this thesis.

5.3 Temperature-Dependent Measurements

The Kerr rotation signal lasts very long ($\sim$ 80 ns) at low temperature (10 K). To determine the origin of the slow decay Kerr rotation signal, temperature-dependent TRKR measurements are performed. The TRKR results at 5 K, 30 K, 75 K and 100 K are shown in Figure (5.7).

As the temperature increases, the Kerr rotation decay time becomes shorter. The

[3]If A_0 is large, τ_3 would be small, vice versa.

[4]The standard error of the fitting parameter is smaller if the data more spread out. This can be seen clearly in the linear regression model $Y = \beta_0 + \beta_1 X + \epsilon$, where Y is response and X is predictor, and ϵ is a mean-zero random error that follows $N(0, \sigma^2)$. Using least square method, we can get $\hat{\beta}_0$ and $\hat{\beta}_1$. The corresponding standard error is $SE(\hat{\beta}_0)^2 = \sigma^2(\frac{1}{n} + \frac{\bar{x}^2}{\sum_{i=1}^{n}(x_i - \bar{x})^2})$ and $SE(\hat{\beta}_1)^2 = \frac{\sigma^2}{\sum_{i=1}^{n}(x_i - \bar{x})^2}$ respectively.

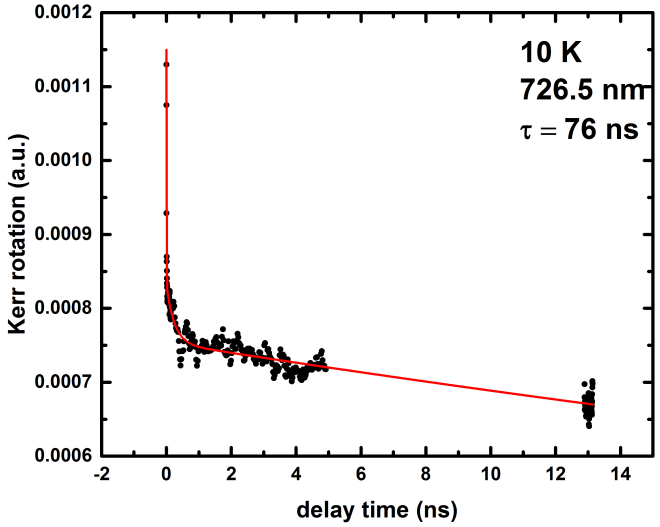

Figure 5.6: The same TRKR data as Figure (5.4). The fitting is done with the negative delay points included.

decay time changes from 75 ns at 5 K to 6 ns at 100 K. The dynamics close to zero delay also change at different temperatures. For TRKR data at 10 K (Figure (5.4)), 30 K and 75 K, the curve can be fit well with three exponential decays. The characteristic time of the fast decay is about several picoseconds, which captures the sharp decay right after pump excitation. The slow decay is tens of nanoseconds, which looks like a straight line in our delay scan window. The intermediate decay time scale is about hundreds of picoseconds which gives a smooth connection between the sharp decay and the slow decay.

The very fast decay can be attributed to the neutral exciton recombination. Time-resolved photoluminescence measurements showed that the neutral exciton recombination time is within several picoseconds in monolayer WSe_2 [39]. Whether the short neutral exciton emission time is limited by radiative recombination or by nonradiative processes is still an open question.

The intermediate decay does not show up at either very low or high temperature. At 5 K and 100 K, the fast decay is followed directly by the slow decay. Experiments

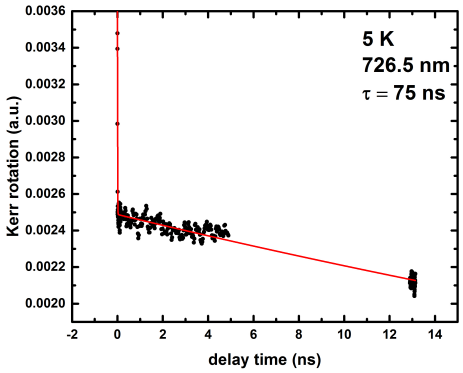

(a) TRKR at 5 K, $\lambda = 726.5$ nm

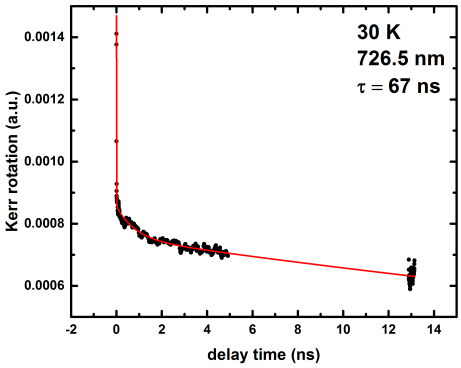

(b) TRKR at 30 K, $\lambda = 726.5$ nm

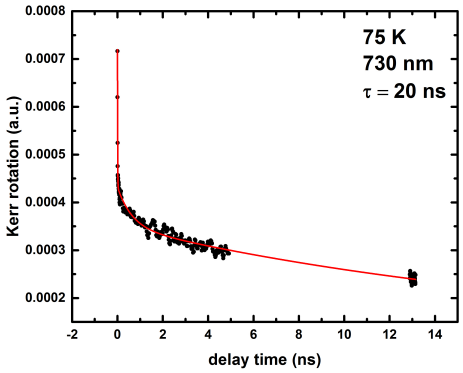

(c) TRKR at 75 K, $\lambda = 730$ nm

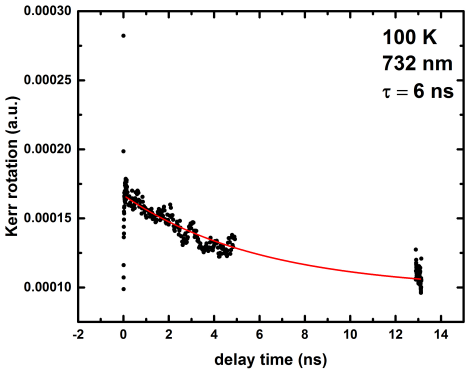

(d) TRKR at 100 K, $\lambda = 732$ nm

Figure 5.7: TRKR of monolayer WSe_2 (sample WSe64-9) at 5 K, 30 K, 75 K and 100 K. The slow decay times τ_3 extracted from the fits are also shown for each temperature. Both the decay time and the signal amplitude decrease with increasing the temperature. The TRKR at 30 K and 75 K are fit with three exponential decays (Eq (5.2)). The TRKR at 5 K is fit with two exponential decays. The 100 K data is fit with one exponential decay.

have shown that the trion recombination time is about tens of picoseconds which is close to the intermediate decay time observed in our experiments [39, 40]. If the intermediate decay is due to trion recombination, the absence of the intermediate decay at 100 K can be explained as follows: At high temperatures, the kinetic energy of the extra charge in the trion becomes comparable to the trion binding energy (tens of meV) [41, 42]. The trion is more likely to lose the extra charge and becomes a

neutral exciton. However, this could not explain the data at 5 K (where no apparent intermediate decay is observed either). Unfortunately, for both WSe_2 samples, the trion peak does not show up in temperature-dependent photoluminescence measurements due to the very broad localized exciton peak. The origin of the intermediate decay is still an open question. In this thesis, I will focus on the slow decay.

When the decay time scale is much larger than the delay scan window, TRKR measurements can be inaccurate. In our TRKR measurements, the delay scan range is about 5 ns, which corresponds to more than 1-meter travel range of the mechanical delay line. The possible light intensity change due to the delay line moving could result in an inaccurate measurement of decay time. An alternative is performing spatially-resolved Kerr rotation measurements at two delay times that are far from each other but physically close. By comparing the Gaussian height of the scan results, the decay time can be estimated.

Here the spatially-resolved Kerr rotation measurements are performed at 1 ns and -200 ps (12.95 ns). These two points are physically close on the delay line, which minimizes the issue of intensity change due to the moving of the delay line. 1 ns is chosen so that the complicated fast and intermediate decay can be excluded. Figure (5.8) shows the results of spatially-resolved measurements at 5 K, 30 K, 75 K, and 100 K.

At low temperatures (5 K and 30 K), the Gaussian height at 1 ns delay is very close to that at -200 ps delay, which means most of the Kerr rotation signal still exist 13 ns after the excitation. At higher temperatures (75 K and 100 K), it is apparent that the relative height between the -200 ps curve and 1 ns curve decreases which is a sign of lifetime decreasing.

The slow decay time can be extracted from the spatial-resolved Kerr rotation measurements assuming the Kerr rotation signal follows a single exponential decay. The Kerr rotation signal generated by the most recent pump pulse is:

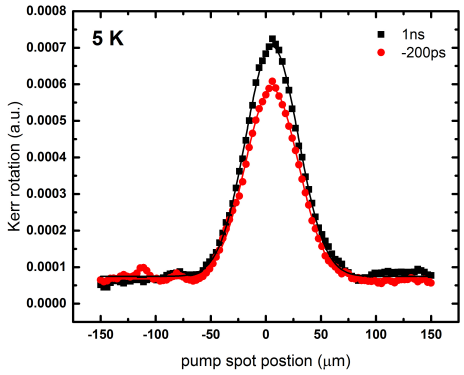

(a) Spatial-resolved Kerr rotation at 5 K, λ = 726.5 nm

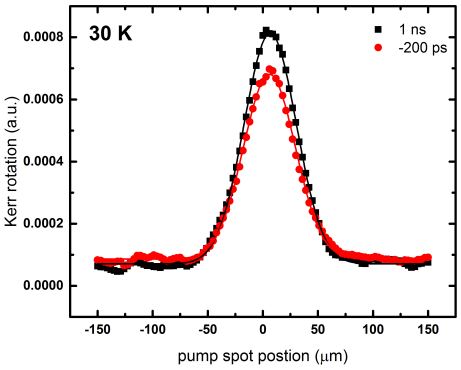

(b) Spatial-resolved Kerr rotation at 30 K, λ = 726.5 nm

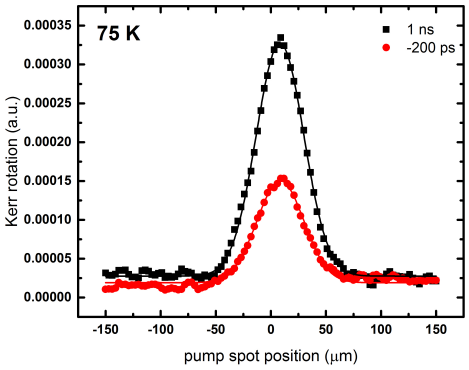

(c) Spatial-resolved Kerr rotation at 75 K, λ = 730 nm

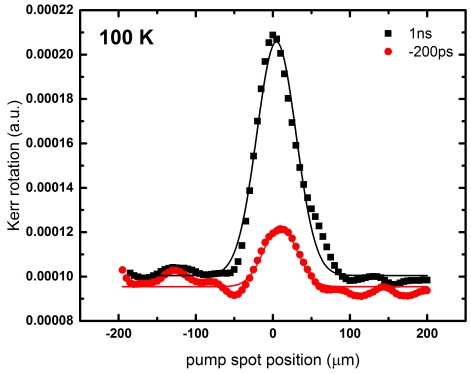

(d) Spatial-resolved Kerr rotation at 100 K, λ = 732 nm

Figure 5.8: Spatial-resolved Kerr rotation of monolayer WSe_2 (sample WSe64-9) at 5 K, 30 K, 75 K and 100 K. The black squares represent data at 1 ns delay and the red dots represent data at -200 ps. The solid lines are fits using a Gaussian curve.

$$A_{single}(t) = A_0 e^{-t/\tau_3} \tag{5.3}$$

where t is the time delay between the pump and probe and τ_3 is the characteristic time of the slow decay. Since τ_3 is much longer than the laser repetition period (t_{rep}), the effects from all the previous pulses should also be taken into account. The Kerr rotation signal probed by the current probe is the summation of signals generated by all the earlier pulses. Using the geometric series summation formula, the result can

be expressed analytically.

$$\begin{aligned} A(t) &= A_0 \sum_{i=0}^{\infty} e^{-(t+it_{rep})/\tau_3} \\ &= A_0 e^{-t/\tau_3} \sum_{i=0}^{\infty} e^{it_{rep}/\tau_3} \\ &= A_0 \frac{e^{-t/\tau_3}}{1 - e^{-t_{rep}/\tau_3}} \end{aligned} \tag{5.4}$$

If the Kerr rotation amplitude is measured at two different delay times t_1 and t_2, the slow decay time τ_3 can be calculated using Eq (5.4):

$$\tau_3 = \frac{(t_2 - t_1)}{ln(A(t_1)/A(t_2))} \tag{5.5}$$

In our case, $t_1 = 1$ ns, $t_2 = 12.95$ ns $A(t_1)$ and $A(t_2)$ are the Gaussian amplitude at 1 ns and 12.95 ns. The slow decay time extracted from TRKR and spatial-resolved Kerr rotation at different temperatures are shown in Figure (5.9).

The slow decay time extracted from the TRKR and spatial-resolved Kerr rotation are close. The error bars of the black circles (spatial-resolved Kerr rotation) is the standard deviation of the decay time of a few runs (5-7 runs). The error bars of the red triangles (TRKR) is the upper and lower bound of the decay time using the lowest and highest background offset[5].

5.4 The Origin of the Slow Decay Kerr Rotation Signal

The lifetime of the slow decay in our Kerr rotation signal is on the order of tens of nanoseconds which far exceeds exciton (a few picoseconds) and trion ($\sim$ hundreds

[5]As we mentioned in Chapter 5.2, the slow decay time is correlated with the background offset, which needs to be fixed when fitting τ_3. The background offset is obtained from spatial-resolved Kerr rotation measurements. The background offests differ slightly between runs. Using the largest background offset in TRKR fitting gives the lower bound of τ_3. Whereas using the smallest one gives the upper bound.

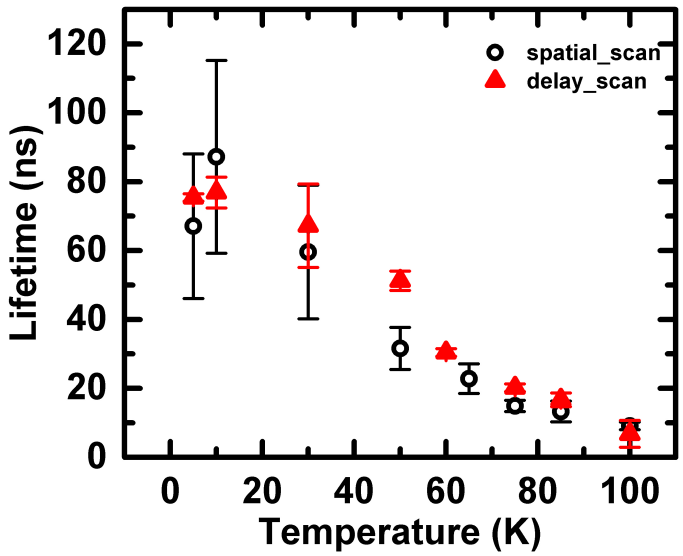

Figure 5.9: The slow decay time extracted from TRKR (red triangles) and spatial-resolved Kerr rotation (black circles). The measurements are done on sample WSe64-9.

of picoseconds) recombination times from time-resolved photoluminescence measurements [39, 43]. The Kerr rotation signal arises from the circular dichroism of the right and left circularly polarized light. Any carrier imbalance that causes a shift in the absorption edge of the right and left circularly polarized light will lead to a Kerr rotation. For example, in n-type GaAs, the Kerr rotation signal mainly results from electron spin polarization. In TMDs, it is more complicated. Both spin and valley polarization can result in Kerr rotation. Also, because of strong Coulomb interaction, the electrons and holes form quasi-particles such as excitons and trions. Whether a single particle picture is feasible to describe the dynamics is still under investigation. In the meantime, both the polarization of resident holes and dark trions could be the physical mechanism for the long-lived Kerr rotation signal observed in p-type WSe_2. Further study needs to be conducted to nail down the origin of this long-lived signal.

5.4.1 Polarization of Resident Carriers

The Transfer of spin polarization from photo-excited carriers to resident carriers is not unusual. In n-type GaAs, hole spins depolarize much faster than electrons, and the electron spin polarization can exist for a long time after the recombination of photo-excited carriers [34]. The transfer of polarization from photo-excited carriers to resident carriers happens when one type of carrier (electron or hole) has at least partially depolarized before recombination. In such situations, the spin lifetime of the other type of carrier is only limited by spin relaxation process instead of carrier recombination time.

In WSe_2, the conduction band spin splitting is about 30 meV which is much smaller than the valence band splitting ($\sim$ 400 meV)[44]. If we ignore the splitting in the conduction band (we will take into account the conduction band spin splitting later), the long-lived Kerr rotation can be explained by the spin/valley polarization of the resident holes. The transfer of spin polarization from photo-excited carriers to resident holes in WSe_2 is shown schematically in Figure (5.10).

Since the sample is p-doped, before photo-excitation, there is an equal amount of holes in the K and K$'$ valleys. Based on our PL measurements, there are some defect states in the samples, which are denoted by the dashed line in between the conduction band and the valence band. A circularly polarized σ^+ pump pulse generates electrons and holes in the conduction band and valence band in the K valley (Figure (5.10)(b)). The electrons experience very fast inter-valley scattering ($\sim$ hundreds of femtoseconds) and reach equilibrium [45]. On the other hand, the holes stay polarized, and some of them relax to the defect states (Figure (5.10)(d)). Hole depolarization requires both spin flip and momentum change, which is very hard [17]. Most of the electrons radiatively recombine with holes in the defect states based on the strong localized exciton peak in low-temperature PL (Figure (5.10)(e)). After photo recombination, the holes in the valence band are still polarized (Figure (5.10)(f)). Since

there are no more electrons to recombine, the hole spin/valley polarization lifetime is only limited by the hole inter-valley scattering, which requires simultaneous large momentum change and spin-flip. Large momentum change requires atomic-scale scatterers, and spin-flip requires magnetic defects. Therefore, the inter-valley scattering of the holes in WSe_2 is very unlikely. Theoretical calculations show that the hole inter-valley scattering time is on the order of nanoseconds [46].

Under this explanation, the long-lived Kerr rotation signal originates from the resident hole spin/valley polarization. The lifetime measured through TRKR is hole inter-valley scattering time. Note that the above explanation is based on the assumption that there is no spin-splitting in the conduction band and the electron inter-valley scattering is fast. Now we take into account the spin splitting in the conduction band.

5.4.2 Conduction Band Spin Splitting

When the conduction band spin splitting is taken into account, the electrons could have several more configurations. Before discussing those, we first define several quantities here for the convenience of discussion.

The electron spin polarization S_e is the difference between the number of spin-up and spin-down electrons regardless of which valley they are in:

$$S_e = (n_\uparrow + n'_\uparrow - n_\downarrow - n'_\downarrow) \tag{5.6}$$

where the up and down arrows represent the spin orientation. $n_\uparrow$, $n_\downarrow$ represents the number of electrons in the K valley and $n'_\uparrow$, $n'_\downarrow$ represent the number of electrons in the K′ valley. Similarly, electron valley polarization is the difference between the number of electrons in the K and K′ valleys regardless of their spin:

$$V_e = (n_\uparrow + n_\downarrow - n'_\uparrow - n'_\downarrow) \tag{5.7}$$

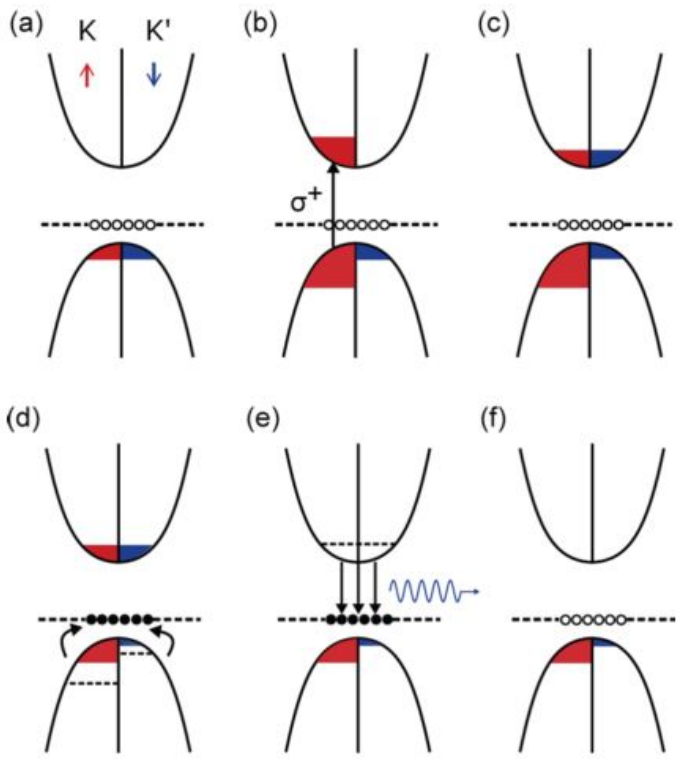

Figure 5.10: The transfer of spin polarization from photo-excited carriers to the resident holes in WSe_2. (a) Some defect states (unfilled circles) are located close to the valence band edge. Before photo-excitation, the defect states are almost empty and the resident holes are not polarized. (b) Circularly polarized light (σ^+) generates spin-up electrons and holes in the K valley. (c) The electrons depolarize because of fast inter-valley scattering. (d) The holes in both valleys nonradiatively decay to the defect states (filled circles). (e) The holes in the defect states radiatively recombine with the electrons in the conduction band, emitting light at the localized exciton emission energy. (f) The resident holes are still polarized after recombination.

For holes, because of the large spin-splitting (∼400 meV in WSe_2), they are very unlikely to be in the lower valence band i.e. spin and valley are inter-locked. The formula of spin and valley polarization are the same (n represents the number of holes here):

$$S_h = (n_\uparrow - n'_\downarrow) \tag{5.8}$$

$$V_h = (n_\uparrow - n'_\downarrow) \tag{5.9}$$

Kerr rotation originates from circular dichroism, i.e., as long as the carrier distribution shifts the absorption curve for σ^+ and σ^- light, a Kerr rotation will be observed. Kerr rotation can originate from different carrier distributions as shown in Figure (5.11). Due to the large spin-splitting in the valence band, the diagram only includes the upper band. The diagram also captures the fact that in tungsten-based TMDs, the spin-splitting in the conduction band and the valence band are the same, i.e., the spin up (spin down) band in both the conduction and valence band have higher (lower) energy than spin down band in the K (K$'$) valley. For simplicity, we assume the material is intrinsic for the discussion here.

With σ^+ excitation, spin-up electrons and holes are generated in the K valley as shown in Figure (5.11)(a). In this case, S_e, S_h, V_e and V_h are all non-zero. Because of Pauli blocking, the absorption edge of σ^+ and σ^- light shift causing a Kerr rotation. In other words, the Kerr rotation measures the "sum" of S_e, S_h, V_e and V_h.

The photo-excited spin-up electrons in the K valley have more scattering channels compared with the conduction-band-spin-degenerate case. Figure (5.11)(b) shows energy-favorable spin-conserved inter-valley scattering (scattering rate is denoted by γ_1) which does not require spin-flip. This spin-conserved inter-valley scattering is fast (on the order of hundreds of femtoseconds to picoseconds). Once the equilibrium is reached, the electron valley polarization V_e is close zero. The electron spin polarization S_e, hole spin/valley polarization S_h and V_h are non-zero. Since σ^+ light couples the spin-up conduction and valence bands in the K valley and there are already electrons and holes in those bands, less σ^+ light is absorbed. On the other hand, there is no electron and hole in the spin-down conduction and valence band in the K$'$ valley; more σ^- light is absorbed resulting in a Kerr rotation. In this case, the Kerr rotation measures the "sum" of S_e, S_h and V_h.

Besides spin-conserved inter-valley scattering, an electron can also have spin-flip inter-valley scattering (scattering rate is denoted by γ_2) as shown in Figure (5.11)(c).

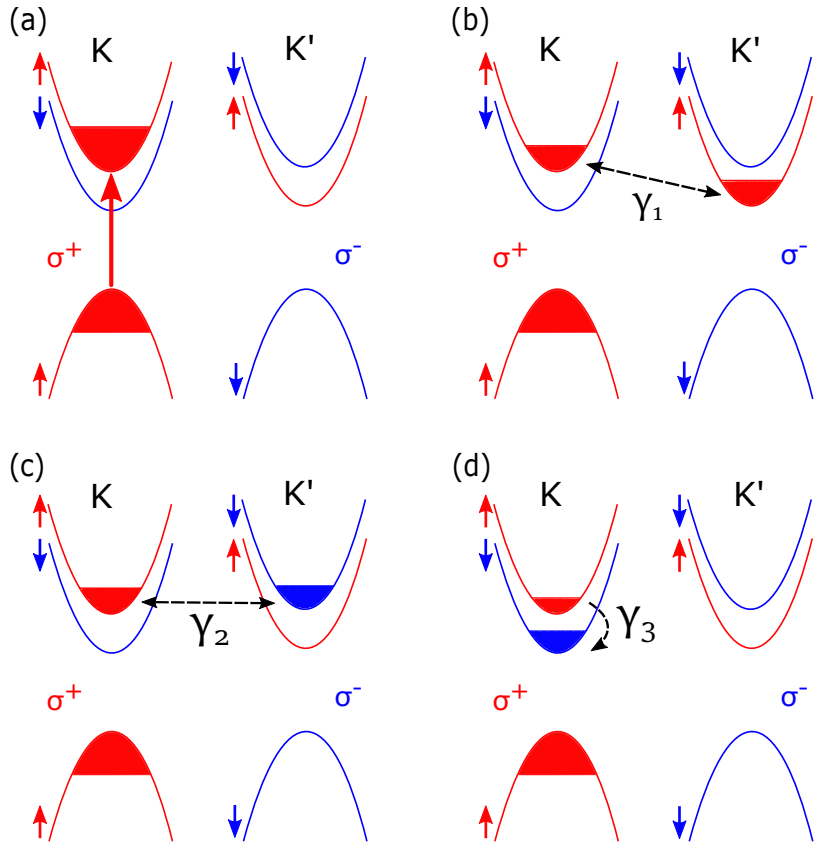

Figure 5.11: Several possible electron and hole distributions that would cause a Kerr rotation. Here we assume the material is intrinsic (no resident carriers). (a) σ^+ light generates spin-up electrons and spin-down holes in the K valley. For electrons, both the spin and valley polarization are non-zero. For holes, the spin and valley polarization are inter-locked and non-zero. Because of the presence of spin-up electrons and holes in the K valley, less σ^+ light is absorbed than $\sigma-$ light causing a Kerr rotation. (b) Electron inter-valley scattering without spin flip decreases valley polarization V_e ($V_e = 0$ in the figure) but not spin polarization S_e. The spin-conserved inter-valley scattering rate is label by γ_1. (c) Electron inter-valley scattering with spin-flip decreases both V_e and S_e ($V_e = 0$ and $S_e = 0$ in the figure). This spin-flip inter-valley scattering rate is label by γ_2. (d) Electron intra-valley scattering decreases spin polarization S_e but not valley polarization V_e. This intra-valley scattering rate is label by γ_3. Temperature-dependent PL shows that γ_3 increases with decreasing the temperature [28].

γ_2 is much smaller than γ_1 since spin-flip and momentum change are required at the same time (similar to hole inter-valley scattering). Moreover, it is not energetically favorable. Assume the electrons reach equilibrium after some time via spin-flip inter-valley scattering[6]. There is no electron spin or valley polarization, i.e., both S_e and

[6]Since γ_2 is small, in reality, this equilibrium may never be achieved. Here I only want to show

V_e are zero. The spin and valley polarization of holes S_h and V_h are non-zero. In this case, Pauli blocking happens for both electrons and holes in the K valley, whereas it only happens to the electrons in the K′ valley. Thus the absorption for σ^+ and σ^- are still different. The non-zero Kerr rotation originates from hole spin/valley polarization S_h and V_h in this case.

Finally, we show that the spin-up electrons in the K valley can also relax via intra-valley scattering, and the scattering rate is denoted by γ_3. The electron intra-valley scattering requires spin-flip but without momentum change and it is energetically favorable. The schematic is shown in Figure (5.11)(d). All the electrons are in the K valley, but they distribute in both the upper and lower conduction bands. S_e is close to zero (in the case shown here) and V_e is non-zero. The Kerr rotation measures the "sum" of V_e, S_h and V_h.

In the real situation, both the inter-valley scattering and intra-valley scattering exist. The electron configuration in the conduction band can be a mix of the configurations shown above. Moreover, electron-hole recombination, either radiatively or non-radiatively, also needs to be considered. For example, if the recombination time between the spin-up electrons and spin-up holes in the K valley is much shorter than $\frac{1}{\gamma_2}$, then the configuration shown in Figure (5.11)(c) would never happen. Now we are going to explain the long-lived Kerr rotation signal with conduction band spin-splitting taken into account.

Since our WSe_2 sample is p-doped, there are equal numbers of resident holes are at equilibrium in the K and K′ valley before photo-excitation. The hole defect states are included in this model since localized exciton emission is observed in the photoluminescence measurements. The holes in defect states are unpolarized, and they can recombine with both spin-up and spin-down electrons. Once the electrons and holes in the K valley are generated by the circularly polarized light, the electrons

that Kerr rotation could result from different electron configurations.

relax to the K′ very fast through spin-conserved inter-valley scattering. The spin-up electrons in the K′ valley cannot recombine with the holes in the same valley because of spin mismatch. However, they can recombine radiatively with the unpolarized holes in the defect states (the recombination rate is denoted by r_1) and emit photons as shown in Figure (5.12)(c). At the same time, the spin-up electrons in the K valley can also recombine with the holes in the defeat states (the recombination rate is denoted by r_2) as shown in Figure (5.12)(d). As the holes in the defect states recombine with the electrons, more holes from the valence band relax to the defect states until the recombination is done. The relaxation rate for the spin-up and spin-down holes are the same. Thus after the photo recombination, the holes in the valence band are still polarized. The long-lived Kerr rotation we saw could originate from this resident hole polarization.

Note that besides photo-recombination with holes in defect states, the photo-excited exciton can also relax through other channels such as direct photo-recombination, non-radiative recombination, and exciton-exciton annihilation.

Direct photo-recombination (the intrinsic recombination rate is denoted by r_0) is not the dominant effect based our photoluminescence data. r_0 could be smaller than γ_1, i.e., most of the photo-excited electrons in the K valley get scattered to the K′ valley before photo-recombination. In fact, the effective direct photo-recombination rate is even much smaller than r_0 because only a small portion of the photo-excited carriers are within the light cone.

The above explanation has an assumption that the non-radiative recombination rate γ_n and exciton-exciton annihilation rate γ_{e-e} are smaller than spin-conserve inter-valley scattering rate γ_1. Otherwise, most of the excitons would recombine non-radiatively or be annihilated in the K valley before the electrons get scattered to the K′ valley. This assumption is verified by time-resolved photoluminescence measurements. Using a rate equation, the time evolution of the number of excitons

after excitation can be described as [43]:

$$\frac{dN}{dt} = -r_0^{eff} N - \gamma_n N - \gamma_{e-e} \frac{N^2}{2} \tag{5.10}$$

where r_0^{eff} is the effective direct photo-recombination time (only the excitons within the light cone can combine radiatively), which is much smaller than r_0. The exciton lifetime measured in time-resolved photoluminescence, on the order of picoseconds [39, 43], is the decay time of the "sum" of the three channels. Thus, the timescale of γ_n and γ_{e-e} have to be at least on the order of picoseconds. On the other hand, the inter-valley scattering rate γ_1 is on the order of hundreds of femtoseconds. This confirms our assumption that most of the electrons get scattered to the other valley before non-radiative recombination or exciton-exciton annihilation.

5.4.3 Quasiparticle Picture

In the single-particle picture, the long-lived Kerr rotation signal is explained by the spin/valley polarization of the resident holes. However, as more studies have been done, people find that the optical behaviors of TMDs are dominated by quasiparticles, i.e., excitons and trions [28, 47]. As we discussed in Chapter 3.3 , an exciton is an electron and hole pair bound by Coulomb interaction. An exciton can also capture an extra charge and becomes a trion if the material is doped. The exciton binding energy is large in 2D TMDs due to less screening effect and electric field lines that extend outside the sample. Studies show that the binding energy is 0.5 to 1 eV [27, 48]. With such a large binding energy, using a single-particle picture to describe the valley/ spin dynamics may not be accurate. For example, in the early days of study, some people believed that the optical excitation generates free electrons and holes first, then they form excitons because of strong Coulomb interaction. Nowadays, it is believed that the bandgap of TMDs is larger than the excitation energy used in most previous studies. It is impossible to generate free electrons and holes with excitation energy

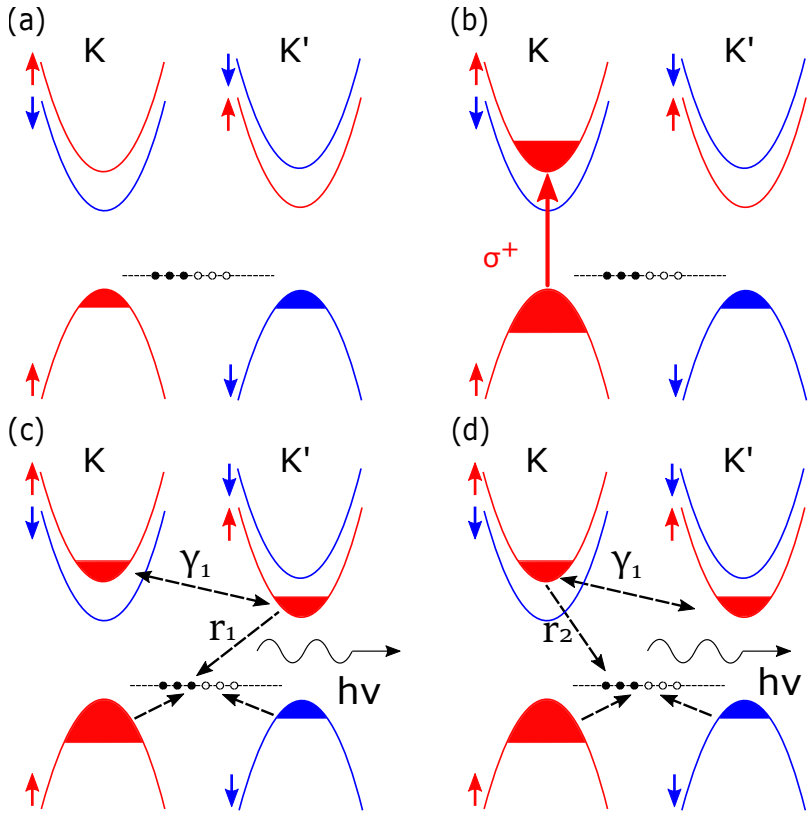

Figure 5.12: The transfer of optically-excited spin/valley polarization to resident holes. (a) p-doped WSe_2 with resident holes in the K and K′ valley. The circles near the valence band edge are hole defect states. (b) σ^+ light generates electrons and holes in the K valley. (c) Electron spin-conserved inter-valley scattering happens between the K and K′ valley. The electrons in the K′ valley radiatively recombine with the holes in the defect states and emit photons (the recombination rate is denoted by r_1). The holes in the K and K′ valleys relax to the defect states. (d) The electrons in the K valley can also radiatively recombine with the holes in the defect states and emit photons (the combination rate is denoted by r_2).

lower than the bandgap. In other words, the optical excitation generates excitons or trions directly with energy much smaller than the bandgap.

In the quasiparticle picture, the origin of the long-lived (tens of nanoseconds) Kerr rotation signal could be dark excitons or dark trions. Because of spin or momentum mismatch, dark excitons and dark trions can not radiatively recombine and thus have a much longer lifetime than their bright counterparts. The lifetime measured in time-resolved photoluminescence is the bright exciton or trion lifetime. How do we measure

the lifetime of dark excitons and trions if they are optically dark? One method is using Kerr rotation. The presence of dark quasiparticles could change the absorption curve of the σ^+ and σ^- light causing a Kerr rotation. The other method is using a very strong transverse magnetic field ($\sim$ 30 T) to tilt the electron spin orientation so that the radiative recombination is weakly allowed [49]. Here I will discuss how to explain the long-lived Kerr rotation signal with dark excitons and dark trions. Since our samples are p-doped, I only focus on the positive trions (exciton with an extra hole). A detailed discussion about negative trions in WSe_2 can be found in this paper [47].

Figure (5.13)(a) shows the generation of the bright excitons with σ^+ light in the K valley. Rigorously speaking, band structure is only valid in the single-particle picture. Thus, although the electron and hole are shown in the conduction band and valence band, they should be considered as an exciton state which is in the bandgap. The energy difference between the exciton state and the conduction band edge is the exciton binding energy. The bright excitons can radiatively recombine and emit photons. The photo recombination time is on the order of hundreds of femtoseconds to picoseconds [45, 39]. The electron could flip spin in the K valley before photo-recombination forming an intra-valley dark exciton as shown in Figure (5.13)(b). The electron in the K valley can also scatter to the lower conduction band in the K$'$ valley forming an inter-valley dark trion. The transition from bright exciton to dark exciton is energetically favorable because of the conduction band spin splitting. This transition is verified by temperature-dependent photoluminescence, where the exciton peak intensity decreases as lowering the temperature [28].

In doped TMDs, optical excitation generates both excitons and trions. The energy difference between exciton and trion is about 30 meV in WSe_2 [50, 51]. In good quality samples where the inhomogeneous broadening is smaller than the trion binding energy, both the exciton and trion peak could be observed in photolumines-

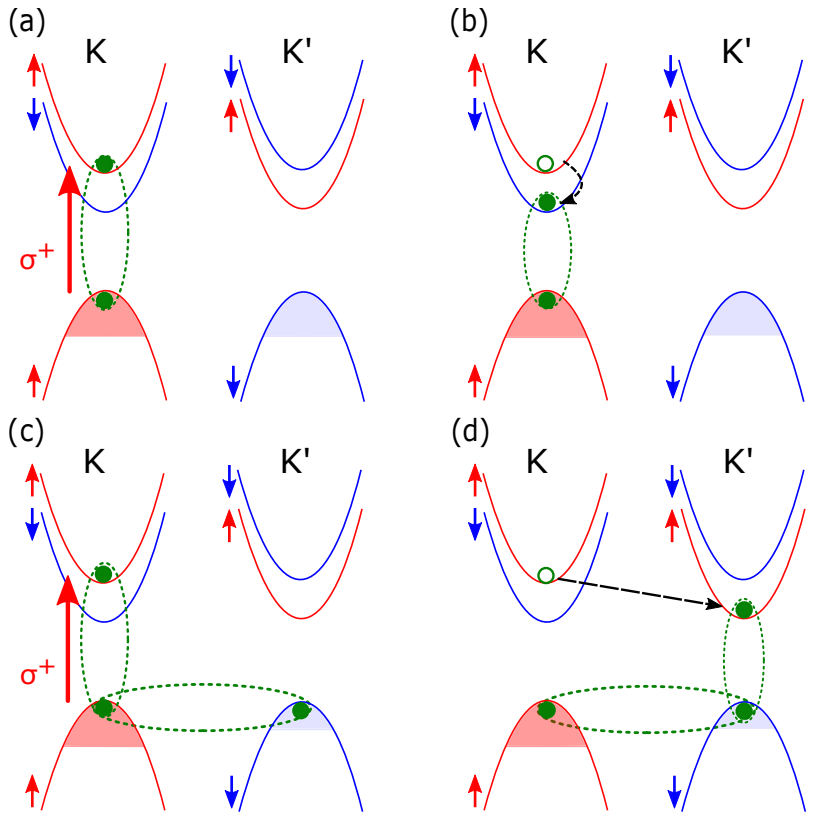

Figure 5.13: Schematics of dark excitons and dark trions formation in monolayer WSe_2. (a) σ^+ light generates bright excitons in the K valley. The excitons are denoted by the green dots and dashed ellipse. The shaded area in the valence band represent the resident holes. (b) The electrons get scattered from the upper conduction band to the lower conduction band and their spin orientation get flipped resulting in dark exciton. (c) σ^+ light generates bright trions. The extra holes in the trions come from the K′ valley resulting in the decrease of holes in the K, valley. (d) The electrons in the K valley get scattered to the K′ valley and dark trions are formed.

cence measurements [51]. Excitons could become dark through electron intra-valley scattering (Figure 5.13(b)) or inter-valley scattering (to the lower conduction band in the K′ valley). Trions could become dark through electron inter-valley scattering (Figure 5.13(c)). Once becoming dark, the exciton and trion can live for a very long time (hundreds of picoseconds to nanoseconds) [47]. Comparing between the dark trion and dark exciton, the dark trion spin/valley polarization lifetime may be longer than that of the dark exciton because the dark exciton could depolarize (inter-valley scattering) through exchange interaction. On the other hand, dark trion inter-valley scattering is unlikely because of Pauli blocking from the hole in the other valley (Figure (5.13)(d)). Therefore, the dark trion is more likely to be the origin of the long-lived Kerr rotation in the quasiparticle picture.

5.5 Magnetic-Field-Dependent Measurements

As we discussed in Chapter 4.1, a transverse magnetic field can be applied while taking TRKR/TRFR measurements. The spin ensemble precesses along the magnetic field at the Larmor precession frequency from which the Lande g-factor can be measured. In monolayer TMDs, the spin behavior under a magnetic field is more complicated. Previous studies on n-type MoS_2 [52, 53] showed a strong magnetic-field-dependent lifetime and a small precession signal. Whereas in n-type WS_2, the lifetime is not sensitive to the magnetic field and there is also a small precession signal [54]. In n-type WSe_2 [47], the Kerr signal contains a magnetic-field-dependent part and a magnetic-independent part.

The explanation of the magnetic-field-dependent lifetime in n-type MoS_2 is the fast inter-valley scattering (the scattering time is at most on the order of picoseconds) and the effective internal magnetic field originated from the conduction band spin splitting. Theoretical calculations show that the conduction band spin splitting is about 0.5-3 meV [55, 44], which corresponds to $\sim$ 10 T internal magnetic field.

Because of the opposite sign of spin-splitting in the K and K′ valley, the effective internal magnetic field directions are opposite for electrons in the K and K′ valley. The electrons in the conduction band experience a fast switch of the internal magnetic field while being scattered between the two valleys. Since the internal magnetic field direction is either parallel or anti-parallel to the spin orientation, there is no spin dephasing. However, once a transverse magnetic field is turned on, the total field (internal plus external) is no longer aligned with the direction of the spins causing the spins to precess. The precession directions are different in the K and K′ valley leading to a D'yakonov-Perel-like spin relaxation mechanism [52]. This explanation relies on fast electron scattering between the K and K′ valley, which might not be possible when the spin-splitting is large. When the splitting is large, instead of scattering between the valleys, the electrons decay from one to the other.

In contrast, in n-type WS_2, the Kerr rotation signal decay time is insensitive to a transverse magnetic field. The conduction band spin splitting in WS_2 is about 30 meV [44], which is more than ten times larger than that in MoS_2. Therefore, the spin-conserved inter-valley scattering between the two valleys becomes a single direction decay. The D'yakonov-Perel-like spin relaxation mechanism with a transverse magnetic field no longer exists. The spin-splitting acts as a large longitudinal internal magnetic field that prevents electron from precessing along the external transverse magnetic field. The small precession signal (less than 3% of the total signal) is attributed to electrons at localized states [54].

In n-type WSe_2, field-dependent Kerr rotation measurements showed two long-lived components. One component is field-independent, and it lasts 150 ns at 5 K, which is attributed to the hole spins in the dark trions. The other component is field-dependent, and it varies as $\frac{1}{B}$, which is attributed to inhomogeneous broadening of the electron spins [47].

In our p-type WSe_2 samples, neither spin precession or magnetic-field-dependent

lifetime is observed. The TRKR measurement results at 10 K with 0, 0.1 and 0.2 Tesla magnetic field are shown in Figure (5.14). The results are very similar (curves are shifted for clarity). The slow decay lifetime extracted from the spatial-Kerr rotation measurements at 50 K with different magnetic fields are shown in Figure (5.15). No apparent magnetic-field dependence is observed.

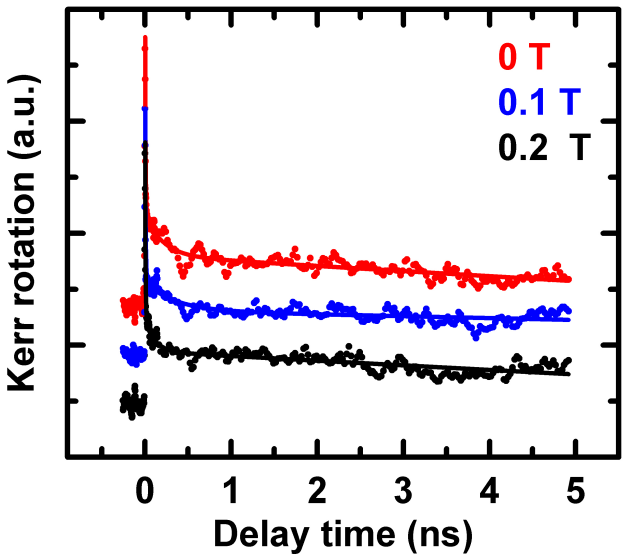

Figure 5.14: TRKR results on monolayer WSe_2 (sample WSe64-9) at 10 K with 0 T, 0.1 T and 0.2 T transverse magnetic field. The curves are shifted for clarity.

We discussed two possible explanations for the long-lived Kerr rotation signal: resident holes and dark trions. In both cases, the absence of spin precession can be explained by the large valence band spin splitting. In WSe_2, the valence band spin splitting is about 400 meV [56, 57]. The longitudinal internal magnetic field due to the spin splitting is on the order of 10^3 T[7], which is much larger than the applied transverse magnetic field. Therefore, the resident hole spins or the trion spins are "pinned" along this large effective magnetic field and have little response to the transverse external field.

[7]Suppose the spin-splitting is Δ. The effective internal magnetic field can be estimated by $\frac{\Delta}{g\mu_B}$

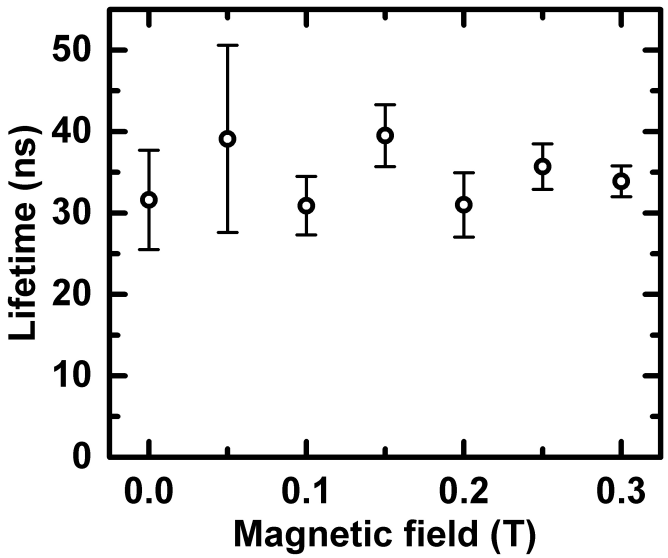

Figure 5.15: The slow decay time extracted from spatial-resolved Kerr rotation measurements at different magnetic fields at 50 K. The error bars come from the standard deviation of the lifetime extracted from multiple runs. The measurements are done on sample WSe64-9.

5.6 Wavelength-Dependent Kerr Rotation Measurements

In Chapter 4.1, we discussed how the Faraday/Kerr rotation amplitude changes with the pump and probe wavelength where the Faraday/Kerr rotation amplitude has two extremums with opposite signs. One of the extremums is below the bandgap, and the other is above the bandgap. In TMDs, the optical transitions are dominated by excitons resulting in much smaller optical excitation energy than the bandgap (a few hundred meV smaller). How the Kerr rotation amplitude changes with the pump and probe wavelength is not apparent with the presence of excitons. Wavelength-dependent Kerr rotation measurements are conducted to gain more information. All the measurements shown later are done in degenerate configuration, i.e., the pump and probe have the same wavelength.

The simplest method to study wavelength-dependent behaviors is measuring the Kerr rotation amplitude directly at different wavelengths. However, this simple

method is not very accurate because only one data point is collected at each wavelength and it suffers from laser power fluctuations. A better way is performing spatial-resolved Kerr rotation measurements at each wavelength and using the Gaussian height as the Kerr rotation amplitude. In this method, the Kerr rotation amplitude is calculated from more data points which lowers the measurement variance. Specifically, at each wavelength, the delay time between the pump and probe pulse is fixed at 1 ns. The probe position is fixed, and the pump scans over the probe[8]. The Kerr rotation amplitude is measured during the scan.

The pump and probe intensity could also affect the Kerr rotation amplitude. In the linear region, the Kerr rotation amplitude is proportional to both the pump and probe power. To rule out the effects from inconsistent laser power at different wavelengths, the Kerr rotation amplitude is normalized by the pump and probe power at each wavelength. Figure (5.16) shows that there is a linear relation between Kerr rotation amplitude and pump power for pump power less than 1.5 mW. The pump power is below 1.5 mW for all the wavelength-dependent measurements.

Figure (5.17) shows the measurement results at 10 K and 50 K. All the measurements are performed with pump power close to 1 mW and probe power close to 0.4 mW which are within the linear region.

Figure (5.17)(a) shows the spatial-resolved Kerr rotation measurements with pump and probe wavelength at 722 nm, 724 nm and 732 nm at 10 K. The Kerr rotation signal is maximized at 724 nm. The data at each wavelength is fit with a Gaussian curve (solid line), and the Gaussian height (normalized by the pump and probe power) is used to represent the Kerr rotation amplitude at that wavelength. Figure (5.17)(c) summarizes how the Kerr rotation (normalized by the maximum height) changes with the wavelength. The Kerr rotation amplitude peaks around 725 nm. Figure (5.17)(b), (d) show the corresponding measurement results at 50 K.

[8]The scan is along the horizontal direction. The pump and probe are centered in the vertical direction.

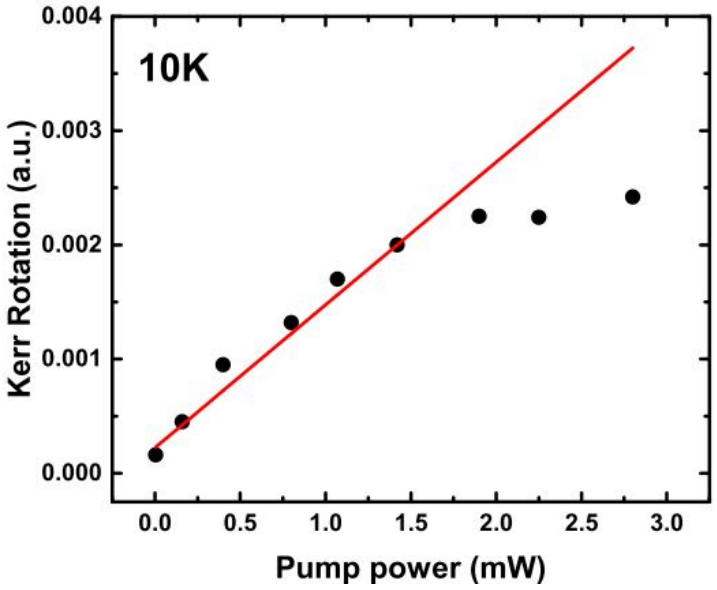

Figure 5.16: Kerr rotation amplitude versus pump power at 10 K. The pump and probe wavelength is 726 nm and the probe power is fixed at 0.37 mW. The Kerr rotation amplitude has a linear dependence with pump power when the pump power is below 1.5 mW. The red line is a linear fit of the data points below 1.5 mW. The measurement is done on sample WSe64-9.

Figure (5.17)(c) and (d) only have one maximum but no minimum which is different from that in classic III-V semiconductors in which a minimum and a maximum with different signs are observed (Figure (4.1)). One possible explanation could be the wavelength window is not large enough to capture the change of sign and the minimum. Due to technical reasons, collecting reliable data at short wavelength is hard[9].

At higher temperatures, the curve shifts to longer wavelength, since the band gap decreases with increasing the temperature. We can perform similar measurements at higher temperatures and hope that the wavelength-dependent Kerr rotation curve shift to longer wavelength so that it is within our laser scan range. We perform measurements up to 110 K, and the results are shown in Figure (5.18). Under 50 K, the maximum Kerr rotation peak position does not change much with temperature, and it is close to 725 nm. Above 50 K, the peak starts to shift to longer wavelength.

[9]The laser does not stay in mode-lock at wavelength shorter than 720 nm.

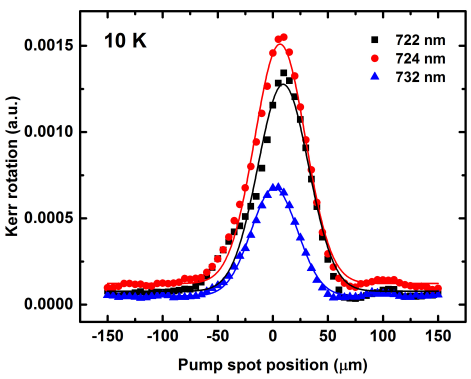

(a) Spatial-resolved Kerr rotation at 10 K for different pump and probe wavelengths.

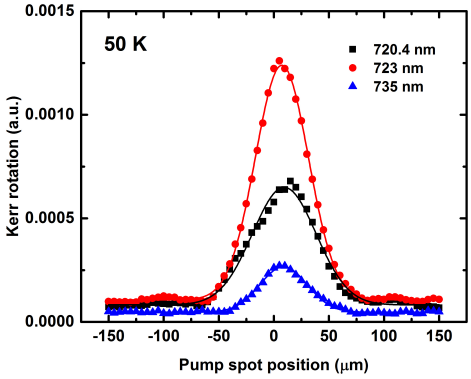

(b) Spatial-resolved Kerr rotation at 50 K for different pump and probe wavelengths.

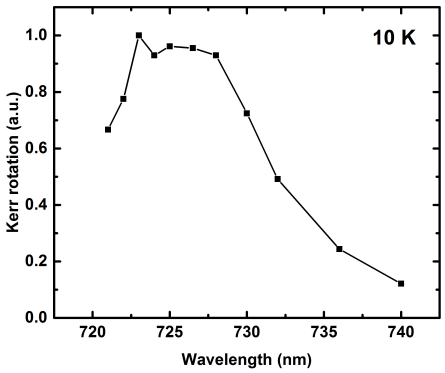

(c) Normalized Kerr rotation amplitude versus pump and probe wavelength.

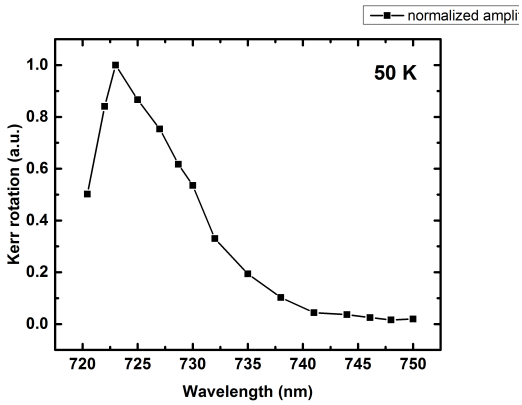

(d) Normalized Kerr rotation amplitude versus pump and probe wavelength.

Figure 5.17: (a), (b): Spatial-resolved Kerr rotation measurement at different wavelength at 10 K and 50 K respectively (Not all the wavelengths are shown). The delay time between the pump and probe is 1 ns. The solid curves are the Gaussian fits. (c), (d): Normalized Kerr rotation amplitudes at different wavelengths at 10 K and 50 K. Each point is a normalized Gaussian height (normalized using the largest Gaussian height) extracted from the spatial-resolved Kerr rotation measurements. The measurements are done on sample WSe64-9.

At 110 K, the maximum Kerr rotation is achieved around 735 nm. However, no Kerr rotation sign change is observed, and the other extremum still does not show up.

Similar experiments are conducted on another MOCVD-grown WSe_2 sample on fused silica with 30 nm SiO_2 layer (WSe90-6-2). More interesting trends show up.

First, the dispersion-Lorentzian shape curve is observed (two extremums with

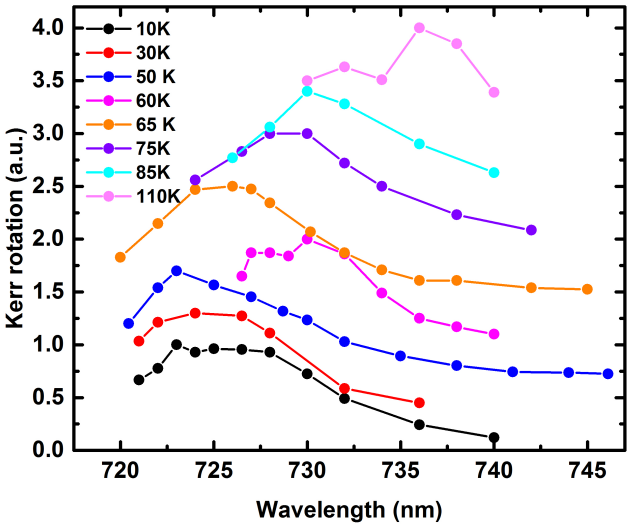

Figure 5.18: Wavelength-dependent Kerr Rotation at Different Temperatures (sample WSe64-9). At each temperature, the curve is normalized by the maximum Kerr rotation amplitude. The curves are shifted for clarity.

opposite signs), which is in line with the theoretical calculation we derived in Chapter (4.1). Figure (5.19)(a) shows the Kerr rotation amplitudes at different pump and probe wavelengths at 10 K, 30 K, and 50 K. At higher temperatures, the curves shift to longer wavelength and their amplitude decrease.

Second, the spatial-resolved Kerr rotation shows complex behaviors near the transition wavelengths where the Kerr rotation changes sign: the sign of the Kerr rotation becomes spatial-dependent. Figure (5.19)(b) shows the spatial-resolved Kerr rotation measurement results near the transition wavelength at 10 K. On either side away from the transition wavelength (for example 736 nm, 742 nm in Figure (5.19)(b)), the curves are Gaussian and centered around zero. However, when the pump and probe are close to the transition wavelength, the curves are no longer Gaussians. Instead, another extremum appears, and the curve becomes anti-symmetric at the transition wavelength (740.4 nm).

One possible explanation for this unusual Kerr rotation amplitude could be the

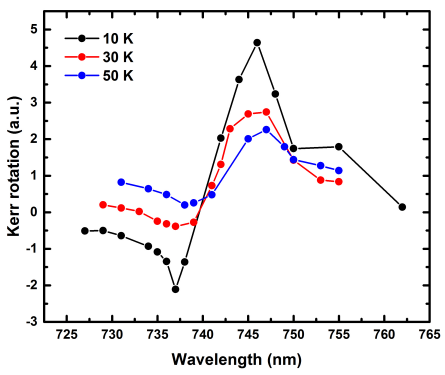

(a) Kerr rotation amplitude versus wavelength at 10 K, 30 K and 50 K.

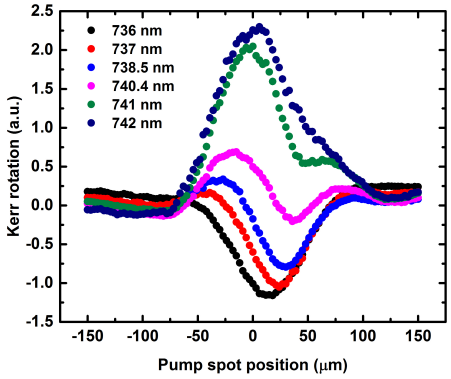

(b) Spatial-resolved Kerr rotation measurements near the transition wavelength at 10 K.

Figure 5.19: (a): Wavelength-dependent Kerr rotation amplitude at 10 K, 30 K and 50 K. The data points are extracted from the Gaussian fits of the spatial-resolved Kerr rotation measurements (normalized by the pump and probe power). (b): Spatial-resolved Kerr rotation measurements near the transition wavelength at 10 K. The delay time between the pump and probe is 1 ns. The measurements are done on sample WSe90-6-2.

spatial chirp of our laser [58]. To keep the model from being too complicated, we assume only the probe frequency has a spatial distribution. Assume the center of the probe spot has frequency w_0, and the frequency at the high and low-frequency side is $w_0 + \delta w$ and $w_0 - \delta w$ respectively. When the center frequency is far away from the transition frequency, the Kerr rotation probed at $w_0 - \delta w$ and $w_0 + \delta w$ has the same sign. Thus the spatial-resolved Kerr rotation curve is close to a Gaussian. However, as w_0 is close to the transition frequency, it is possible that $w_0 - \delta w$ is lower than the transition energy whereas $w_0 + \delta w$ is higher than the transition energy resulting in Kerr rotation with opposite sign.

Figure (5.20) is a schematic of scanning a pump pulse over a spatially-chirped probe. Suppose the probe center frequency w_0 is set at the transition frequency. At the first frame, only the $w_0 - \delta w$ frequency part overlaps with the pump. At the third frame, only the $w_0 + \delta w$ frequency part overlaps with the pump. Since w_0 is the transition frequency, i.e., the Kerr rotation signal is zero at w_0, the Kerr rotation

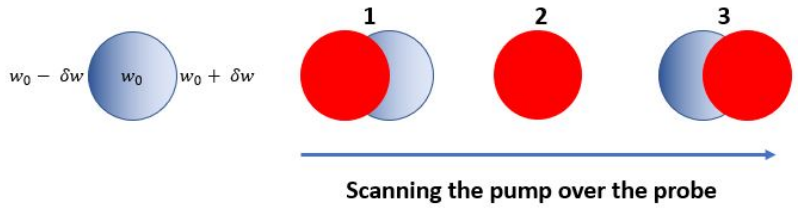

Figure 5.20: Schematic of scanning a pump (red) over a spatially-chirped probe. The probe spot (blue) has a spatial frequency distribution (indicated by the color gradient). The frequency in the pump center is w_0. The frequency on the high and low frequency side is $w_0 + \delta w$ and $w_0 - \delta w$ respectively.

at the first frame and the last frame have different signs. At the second frame, the pump overlaps with the probe completely. The positive and the negative Kerr rotation signal cancel out and the probed Kerr rotation is zero.

Finally, we compare the maximum Kerr rotation energy and the free and local exciton emission energy from the photoluminescence measurements at different temperatures. The localized and free exciton peak positions are extracted from Figure (5.1).

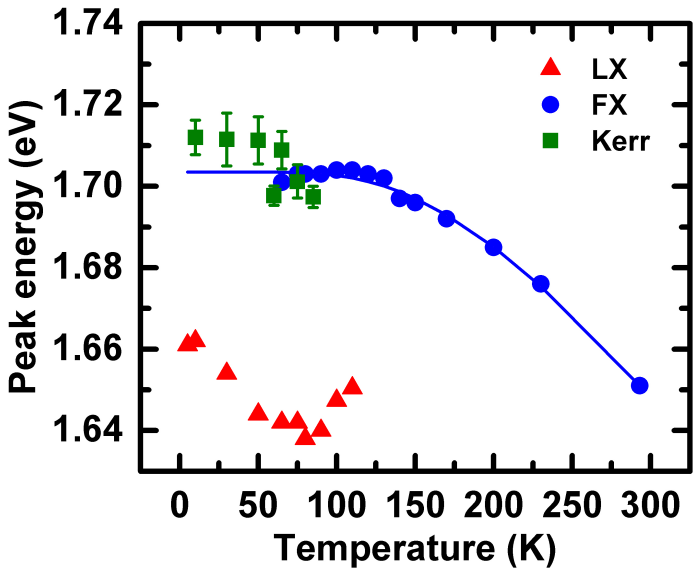

Figure 5.21: Peak positions of Kerr rotation (green squares), localized exciton (red triangles) and free exciton emission at different temperatures. The blue line is a fit using temperature dependent bandgap formula Eq (5.1).

The Kerr rotation peak position (photon energy that maximizes the Kerr rotation amplitude) is very close to the free exciton peak. No Kerr rotation is observed when the laser energy is tuned close to the localized exciton peak. One possibility could be the valley-dependent optical selection rules no longer hold for the defect states, and almost no spin/valley polarization is generated.

We already saw previously that the intermediate decay (decay time on the order of several hundred picoseconds) is temperature dependent on sample WSe64-9. At 100 K and 5 K, the intermediate decay does not show up. It is unclear what is the origin of the intermediate decay. On sample WSe90-6-2, the intermediate decay is wavelength-dependent. At 737 nm, the intermediate decay is observed. Whereas at 746 nm, the intermediate decay no longer exists. Further study is needed to find out the physical origin of this intermediate decay

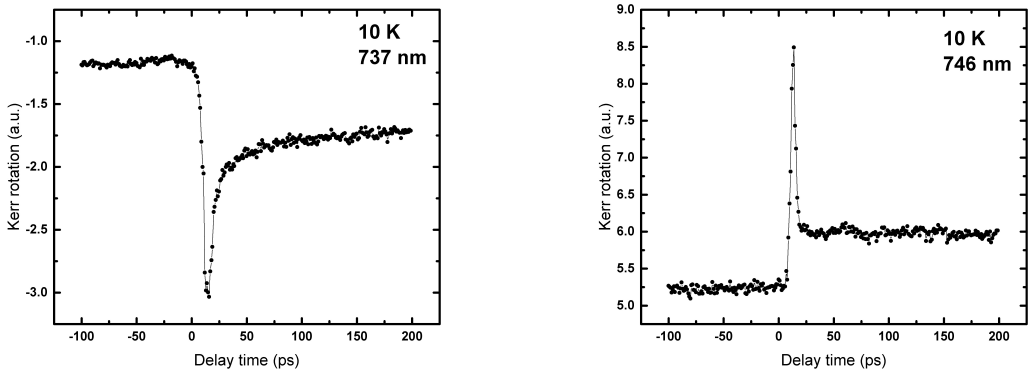

(a) TRKR near zero delay at 10 K with 737 nm pump and probe

(b) TRKR near the zero delay at 10 K with 746 nm excitation

Figure 5.22: Polarization dynamics near the zero delay with 737 nm (a) and 746 nm (b) pump and probe. At 737 nm, there is an intermediate decay (tens of picoseconds) between the fast decay (a few picoseconds) and the slow decay (tens of nanoseconds). At 746 nm, no intermediate decay is observed.

CHAPTER VI

Time-Resolved Kerr Rotation Microscope

6.1 Motivations

In spintronic devices, information is represented by carrier spins. Thus, people want to find materials with long spin lifetime, which sets the upper bound of how long the information can persist. Besides long spin lifetime, an ideal material should also have large spin mobility so that the spin polarization can travel far enough spatially to transfer information. In Chapter V, we showed that monolayer WSe_2 has a long valley/spin polarization on the order of tens of nanoseconds at low temperature. A natural follow-up question is how far this valley/spin polarization can travel spatially in monolayer WSe_2. Spin drag measurements are often used to measure spin drift in semiconductors. In spin drag measurements, a voltage is applied to the sample so that the spin packet generated by the pump beam drifts spatially. The probe beam measures how far the packet travels from where it is generated. Therefore, the smaller the beam size, the better spatial resolution we will have in spin drag measurements. In the TRKR setup I used in Chapter V, the pump and probe beam are focused on the sample by a 150 mm focal length lens. The spot size on the focal point is about 30 microns, which is good enough to measure spin drift in bulk materials. However, the size of an exfoliated monolayer WSe_2 flake is about 10 microns, which is beyond the resolution of our TRKR setup. On the other hand, an objective can focus the

beam down to 1-2 microns which is a powerful tool to study spin drift and diffusion in monolayer WSe_2. At the same time, a new liquid helium cryostation was purchased. My project is to build a time-resolved Kerr rotation microscope(TRKM) setup on this new cryostation. Despite several unique features, the TRKM setup is similar to the TRFR/TRKR setup. In this chapter, I first focus on these unique features and discuss some technical tricks. Then I will move to the calibration measurements performed on the TRKM setup.

6.2 New Features in the TRKM Setup

6.2.1 4f Scanning System

In the TRKR setup, the pump beam spatial scan is realized by changing the angle of the steering mirror before the focusing lens. The steering mirror changes the incident angle of the pump beam resulting in a spatial movement on the focal plane as shown in Figure (6.1).

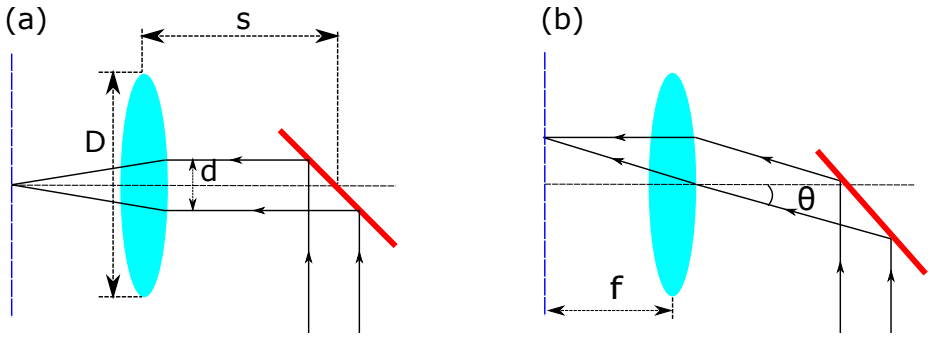

Figure 6.1: Scan the laser spot on a sample with a steering mirror (red line). (a) The incident laser (black lines) is perpendicular to the focusing lens (blue ellipse). The focal plane is represented by the blue dash line. The diameter of the lens D, beam diameter d and the distance between the lens and steering mirror s are shown. (b) Tuning the focusing point on the focal plan by changing the steering mirror angle.

How far the laser spot can move on the sample is determined by the largest incident angle of the beam. In Figure (6.1)(b), the incident angle of the beam is θ with respect to the optical axis. Suppose the focal length is f, the distance moved on the focal

plane is $f\tan(\theta) \approx f\theta$ (usually θ is much smaller than 1). The upper bound of θ is limited by the diameter of the lens. If we ignore the boundary effect of the lens, the upper bound $\theta^\star$ is determined by:

$$\theta^\star = arctan(\frac{D-d}{2s}) \tag{6.1}$$

where D is the lens diameter and d is the incident beam spot diameter. If θ goes beyond $\theta^\star$, part of the incident beam will miss the lens causing an intensity drop. In our TRKR setup $s \approx 650$ mm, $D \approx 25$ mm, $d \approx 2$ mm and $f = 150$ mm. Plugging in these numbers in Eq 6.1, we have $\theta^\star = 0.018$. Therefore, the scanning radius on the sample is $f\theta^\star = 2.7$ mm. We usually perform spatial scans on the order of hundreds of microns which is smaller than the scanning radius. However, when an objective (aperture ≈ 3 mm) is used, the corresponding $\theta^\star_{obj} \approx 8 \times 10^{-4}$. In addition, the objective working distance is shorter than a lens, which is 17 mm in our case. Therefore, the estimated largest scanning radius is only 13 micron. If we scan the steering mirror beyond this limit, part of the incident light will be blocked by the aperture causing an intensity drop. To restore the scanning range, we should be able to change the beam incident angle without changing its incident position on the aperture. The solution is to use a 4f system. 4f systems are broadly used in Fourier optics, such as building low and high pass filters. Here, we are not utilizing the Fourier properties but the geometric properties of a 4f system. Figure (6.2) is a schematic of our 4f system.

Instead of going directly to the objective, the reflection beam from the steering mirror first goes through a pair of confocal lenses. The steering mirror is at the front focus of the first lens and the objective's aperture is at the back focus of the second lens. In this configuration, each beam that passes through the front focus of the 4f system is guaranteed to pass through its back focus regardless of its incident angle. Figure (6.2) shows how the incident angle is changed by tuning the angle of the

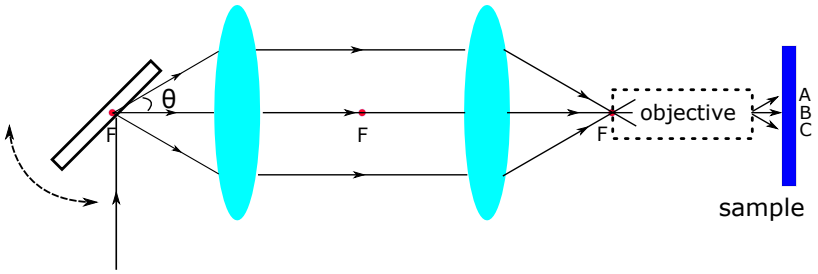

Figure 6.2: Schematic of the 4f system. The steering mirror is at the front focus of the first lens. The back focus of the first lens overlaps with the front focus of the second lens, and they form a confocal lens pair. The aperture of the objective is at the back focus of the second lens. By changing the angle of the steering mirror, the direction of the incident light is changed resulting in a direction change of the out-going light from the objective.

steering mirror. All the three beams pass through the objective aperture and focus on three different positions on the sample. With a 4f system, the incident angle is no longer limited by the objective aperture making it possible to perform large spatial scans on the sample.

To test the scan range and the spot size of our 4f system, reflection measurements are done on a calibration sample which contains 2-dimensional grids on its surface. The side of the square is 8.1 μm, and the channel is 1.9 μm. The schematic and camera image of the calibration sample are shown in Figure (6.3). If the 4f system works as expected, the incident light should not be blocked by the objective's aperture when we scan the steering mirror, and the reflection intensity should be uniform across the scan range. On the contrary, without a 4f system, part of the incident beam is blocked by the aperture causing an intensity drop of the reflection beam.

Figure (6.4) (a) shows the reflection measurement result on the calibration sample with a 4f system. As expected, the reflection shows a periodic pattern. The flat parts correspond to reflection from the squares (the whole beam spot is on one of the squares). When the beam spot starts hitting the edge of the squares, the reflection intensity starts to drop sharply. The peaks between the plateaus correspond to reflection from the channel center. If the spot size is smaller than the channel width,

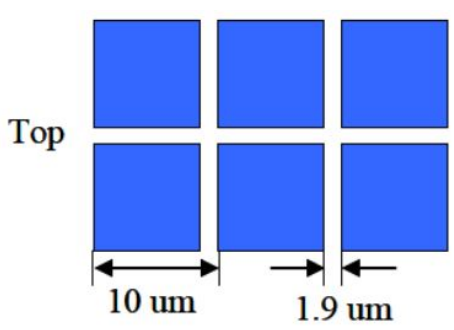

(a) Schematic of the calibration sample.

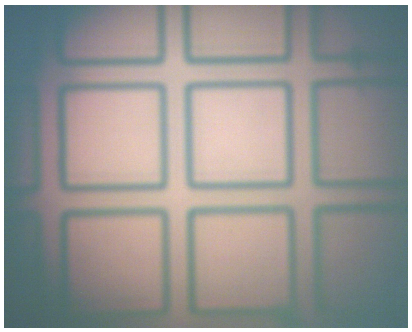

(b) Camera image of the calibration sample.

Figure 6.3: The schematic and camera image of the calibration sample.

the peak height should be the same as the plateau (reflection from the square). In our case, the peak height is lower than the plateau, which means our spot size is larger than the channel width (1.9 μm). Later, we will show how to estimate our spot size from the reflection measurements. Looking at Figure (6.4) (a), it is clear that the plateaus stay at the same height within about 60 μm scanning range, which is large enough for our future measurements. Figure (6.4) (b) shows the reflection measurement result without a 4f system. The steering mirror is placed very close to the objective (s = 100 mm). The intensity changes during the scan because part of the incident light is blocked by the aperture. Figure (6.4) (c) (d) show the results when the distance between steering mirror and objective is far (s = 2000 mm). In these cases, we can not even observe a plateau. The intensity drops quickly when the incident angle deviates from zero. At 250 steps, all the incident light is blocked by the aperture. Whereas in the 4f system, there is no intensity change all the way up to 1000 steps.

6.2.2 Spot Size Estimation

The spot size is estimated through the reflection measurements. Here we show two different methods to do it.

The first method utilizes the fact that the reflection intensity drops if part of the

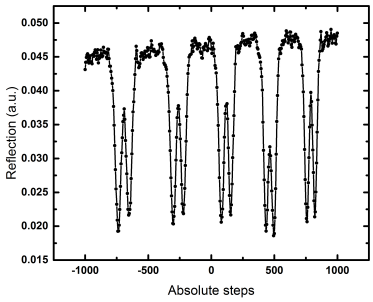

(a) Reflection intensity versus steering mirror moving steps with a 4f system.

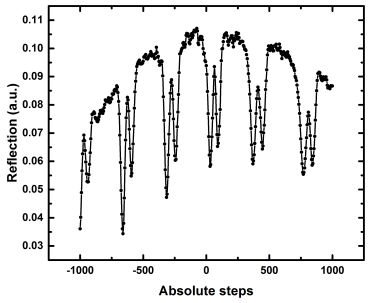

(b) Reflection intensity versus steering mirror moving steps without a 4f system. The distance between the steering mirror and the objective aperture is 100 mm.

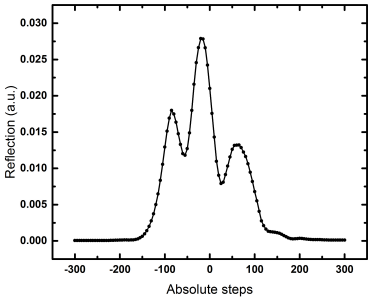

(c) Reflection intensity versus steering mirror moving steps without a 4f system. The distance between the steering mirror and the objective aperture is 2000 mm. The center peak corresponds to the channel on the calibration sample. The two side peaks correspond to the flat squares on both sides of the channel.

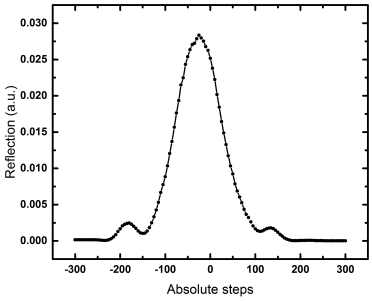

(d) Reflection intensity versus steering mirror moving steps without a 4f system. The distance between the steering mirror and the objective aperture is 2000 mm. The center peak crosponds to the flat sqaure and the two side peaks corespond to the two channels on both sides of the square.

Figure 6.4: Comparison of spatial scans with and without a 4f system.

beam is in the channel. According to Figure (6.5) (a), it takes 365 steps to move across one period which is 10 μm. And it takes 170 steps to move across the channel which corresponds to 4.7 μm. On the other hand, 4.7 μm corresponds to the sum of the beam diameter and channel width as shown in Figure (6.5) (b). Therefore, the spot diameter d is 4.7 - 1.9 = 2.8 μm.

If the spot size is smaller than the channel width, the peak height should be the

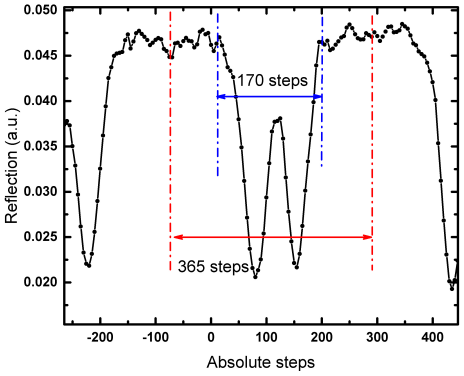

(a) Figure (6.4) zoomed in. One period coresponds to 365 steps and the region where the intensity change coresponds to 170 steps.

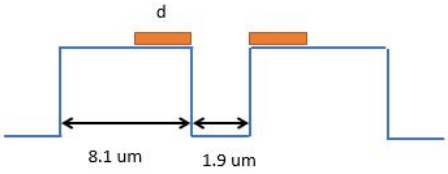

(b) Side view of the calibration sample. The orange rectangle represents beam spot.

Figure 6.5: The first method to estimate the spot size which uses the simple geometry relation between the spot size and channel width.

same as the plateau because no light gets scattered by the channel edge. In our case, the peak height is slightly lower than the plateau as shown in Figure (6.6) (a). Suppose the spot intensity distribution follows a Gaussian distribution, i.e., $I(x) = \frac{1}{\sqrt{2\pi}\sigma} exp(-\frac{x^2}{2\sigma^2})$. When the center of the beam spot is at the center of the channel, only the light inside the channel will be reflected, i.e.:

$$I_{channel} = \int_{-w/2}^{w/2} \frac{I_0}{\sqrt{2\pi}\sigma} exp(-\frac{x^2}{2\sigma^2}) dx \tag{6.2}$$

where w is the channel width and I_0 is the spot total intensity. On the other hand, when the beam spot is totally on the square, the reflection intensity is:

$$I_{square} = \int_{-\infty}^{\infty} \frac{I_0}{\sqrt{2\pi}\sigma} exp(-\frac{x^2}{2\sigma^2}) dx \tag{6.3}$$

It is easy to know $I_0 = I_{square}$ from Eq (6.3). Plug it back into Eq (6.2) and it can be rewritten as:

$$\frac{I_{channel}}{I_{square}} = \int_0^{\frac{w}{2\sqrt{2}\sigma}} \frac{2}{\sqrt{\pi}} exp(-t)dt \tag{6.4}$$

Plug in $I_{channel} = 0.038$ and $I_{square} = 0.047$ and look at an error function table, and we have $\frac{w}{2\sqrt{2}\sigma} = 0.91$. Use w = 1.9 μm and we have $\sigma = 0.74$ μm. Therefore, the beam diameter d = $4\sigma \approx 3$ μm (95% intensity), which is very close to the 2.8 μm we get from the first method.

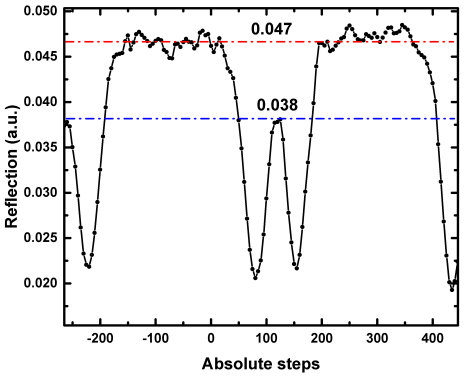

(a) Figure (6.4)(a) zoomed in. The plateau intensity is about 0.047 (red dash line) and that of channel peak is about 0.038 (blue dash line).

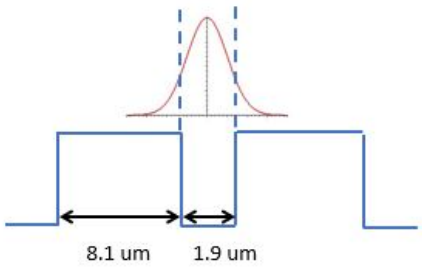

(b) Side view of the calibration sample. The intesity distribution of the beam spot is also shown. We assume the reflection outside of the verticle dash line is not collected by the photo detector.

Figure 6.6: The second method to estimate the spot size which assumes the beam intensity has a Gaussian distribution.

6.3 Test Measurements on the Time-Resolved Kerr Rotation Microscope

Besides having smaller beam size, there is another difference between the TRKM and TRKR/TRFR setup. In the TRKR/TRFR setup, the pump and probe beam are spatially separated. Although there could be some pump scatter, most of the beam collected by the photodiode bridge is the probe light. However, in the TRKM

setup, the objective aperture is so small that both the pump and probe beam pass co-linearly and are collected by the photodiode bridge. In other words, the pump scattering in the TRKM setup is very strong making it hard to get a good Kerr rotation signal. Through careful tunings and adjustments, we achieve an SNR that is comparable to that from the TRFR/TRKR setup. In this section, I will show some Kerr rotation measurement results from the TRKM setup. Then I will compare these results with similar experiments done on the TRKR/TRFR setup. Finally, I will discuss the relation between the measurement geometry (Faraday/Kerr) and the measured spin lifetime.

Two samples are used to test the TRKM setup. One is a bulk GaAs (MTI-001-A2) sample, and the other is a 500 nm Indium-doped GaAs epilayer sample (RMBE-1302-B). We first discuss the results from the GaAs sample then move to the epilayer sample.

Figure (6.7)(a) shows the time-resolved Kerr rotation measurements on the bulk GaAs at 10 K and 300 mT magnetic field with the TRKM setup. The data follows a clear exponential decaying cosine, and the oscillation frequency is the Larmor precession frequency $\frac{g\mu_B}{\hbar}$. This indicates that the signal we observe here originates from the electron spin polarization. However, the spin lifetime extracted from the fit is about 3 ns, which is much shorter than what we measured in the Faraday geometry. This short lifetime measured from the time-resolved scan with the TRKM setup is verified by an RSA scan as shown in Figure (6.7)(b). The RSA scan from the TRKM setup does not have any constructive interference spikes which is a sign of a short lifetime. Figure (6.8)(b) shows RSA measurement result in the Faraday geometry at 10 K on the same sample with the TRFR setup. The lifetime extracted from the fit is about 30 ns. In bulk GaAs, the electron spin lifetime decreases with increasing the temperature [34]. Figure (6.8) shows time-resolved scan at 75 K and 200 mT. The spin lifetime extracted from the fit is about 3 ns.

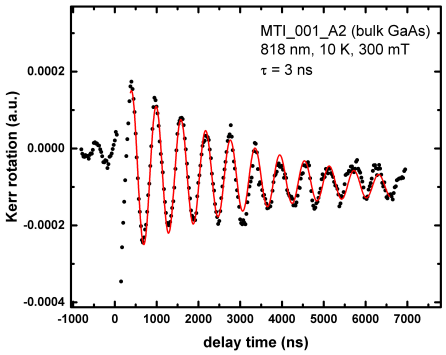

(a) Time-resolved Kerr rotation measurement at 10 K and 300 mT transverse magnetic field. The data can be fit with an exponential decaying cosine and the lifetime is about 3 ns.

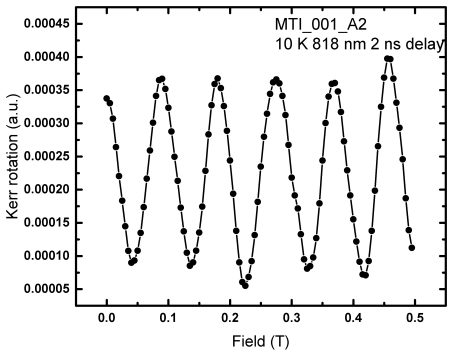

(b) RSA measurement at 10 K and 2 ns delay time.

Figure 6.7: Time-resolved Kerr rotation and RSA measurements on bulk GaAs with the TRKM setup.

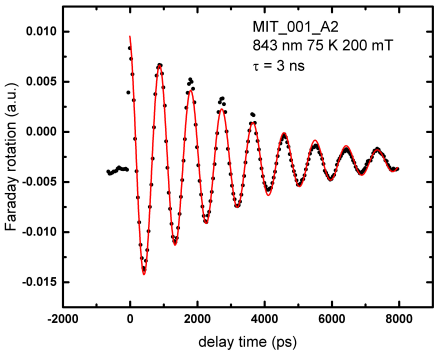

(a) Time-resolved Faraday rotation measurement at 75 K and 200 mT transverse magnetic field. The data can be fit with an exponential decaying cosine and the lifetime is about 3 ns.

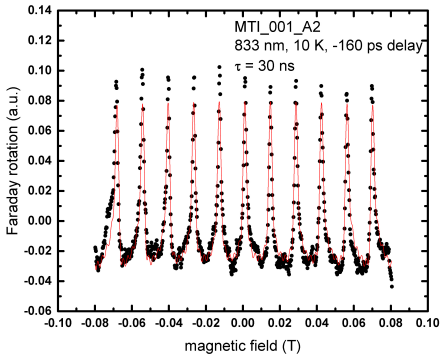

(b) RSA measurement at 10 K and -160 ps delay time.

Figure 6.8: Time-resolved Faraday rotation and magnetic field-dependent measurements on bulk GaAs with the TRFR setup.

The spin lifetime measured from the TRKM setup is much shorter than that from the TRFR setup in both time-resolved scans and magnetic-field scans. Considering the spot size difference between the two setups, one natural explanation is spin diffusion. In pump-probe measurements, the magnitude of the rotation signal

is proportional to the number of carriers within the probe area and carrier spin polarization. The spin diffusion out of the probe area would cause a decrease of the rotation signal. The spin lifetime is estimated by measuring how fast the rotation signal decays. Therefore, spin diffusion makes the measured spin lifetime shorter than the real lifetime, and this effect is stronger for smaller probe size. However, a similar spin lifetime is observed in the Indium-doped GaAs epilayer sample in both the TRKM and TRKR setup. Figure (6.9)(a) and (b) show the time-resolved scan result from the TRKM and TRKR setup at 30 K respectively. The spin lifetimes extracted from both measurements are the same.

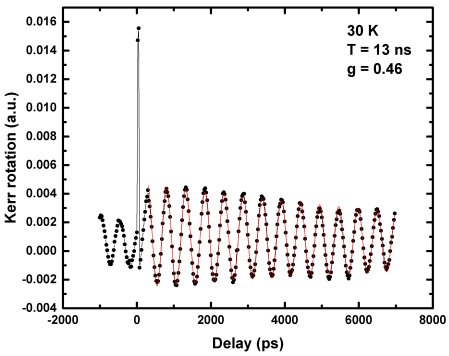

(a) Time-resolved Kerr rotation measurement at 30 K and 300 mT transverse magnetic field on the TRKM setup. The data can be fit with an exponential decaying cosine and the lifetime is about 13 ns.

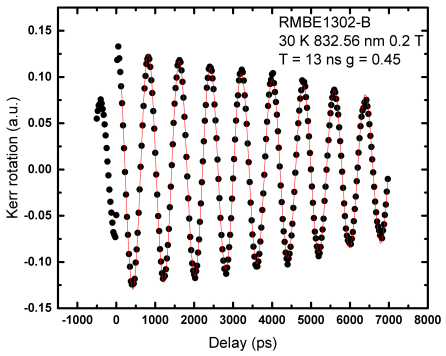

(b) Time-resolved Kerr rotation measurement at 30 K and 300 mT transverse magnetic field in the TRKR setup. The data can be fit with an exponential decaying cosine and the lifetime is also 13 ns which is the same as we measured on the TRKM setup

Figure 6.9: Time-resolved scans on the indium-doped GaAs epilayer sample with the TRKM and TRKR setup

There are two possible explanations for the different results we saw in Figure (6.7), (6.8) and (6.9). One is that the measured spin lifetime could depend on the probe geometry (Faraday or Kerr) and wavelength[1]. The results in Figure (6.7) are measured with Kerr geometry whereas Faraday geometry is used in Figure (6.8). And

[1]The wavelength used in Kerr geometry (reflection) is usually shorter than that in Faraday geometry (transmission). In other words, the measurement geometry and wavelength are coupled.

the measured spin lifetimes differ a lot (3 ns vs 30 ns). The results in Figure (6.9) (a) and (b) are both from Kerr rotation measurements and the lifetimes are the same (13 ns). The other possibility is that the spin diffusion constant in bulk GaAs is larger than that in the indium-doped GaAs epilayer. The spin diffusion is so slow in the indium-doped GaAs epilayer that the probe spot size does not affect the measured spin lifetime[2].

Fortunately, a previous group member measured the spin lifetime of bulk GaAs in Kerr rotation which is shown in Figure (6.10). Although the pump and probe spot size are about 40 microns (much larger than the spot size in the TRKM setup), the spin lifetime is 4.2 ns which is very close to that measured from the TRKM setup (see Figure (6.7)). This supports the first possibility we discussed above, i.e., the measured lifetime depends on the geometry and wavelength.

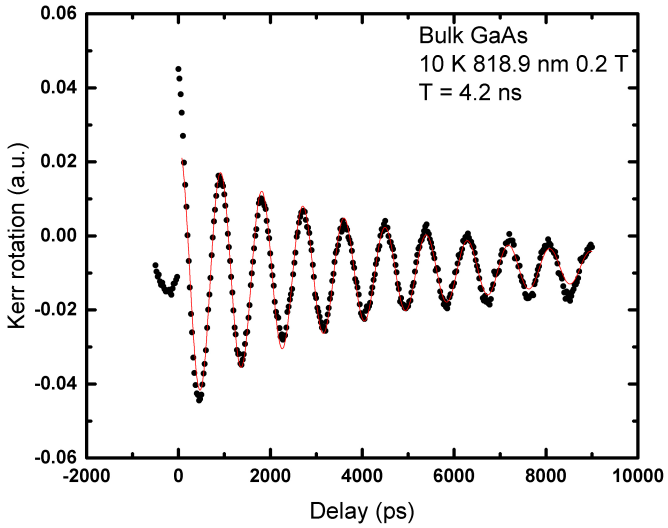

Figure 6.10: Time-resolved Kerr rotation measurement on bulk GaAs. The spin lifetime extracted from the fit is 4.2 ns which is very close that measured from the TRKM setup. (Figure (6.7)).

To test the second possibility (spin diffusion causes the measured spin lifetime

[2]In the extreme case, if there is no spin diffusion, the measured spin lifetime would be independent of the probe spot size.

to be shorter), pump-probe overlap scans at different delays are performed on the bulk GaAs sample with the TRKM setup. If the spin diffusion plays a role here, a Gaussian width change should be observed. Figure (6.11) shows the measurement results. There is no obvious width change from 200 ps to 3 ns, which means that diffusion does not play an important role in explaining the short lifetime we observed in the TRKM setup[3].

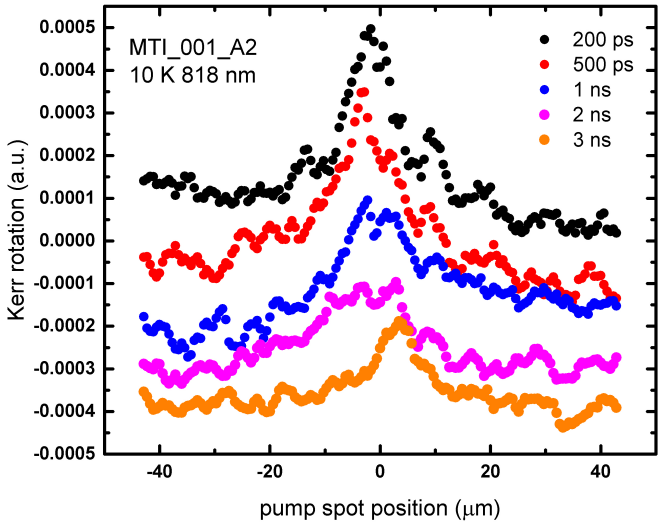

Figure 6.11: Pump-probe overlap scans at different delay times on bulk GaAs on the TRKM setup. The curves are shifted for clarity.

[3]However, this measurement does not rule out the diffusion happens between 0 and 200 ps. Due to technical difficulties, we can not get reasonable signal in this window.

CHAPTER VII

Conclusion

My PhD work focuses on studying spin polarization dynamics in semiconductors with light. Specifically, we use the time-resolved Kerr rotation technique to investigate the spin/valley polarization in p-type monolayer tungsten diselenide (WSe_2). An 80 ns spin/valley lifetime is observed which is the longest spin/valley lifetime in WSe_2 by that time. Two possible physical mechanisms, resident carrier polarization and dark trion polarization, have been proposed to explain the observed long lifetime. Different from traditional semiconductors in which the spin polarization precesses along an external transverse magnetic field, no spin precession is observed in WSe_2 under a magnetic field up to 0.3 T. The robustness to a transverse magnetic field is attributed to the large spin splitting in the valence band due to spin-orbit coupling. Our study shows that WSe_2 could be a promising candidate for future spintronic devices.

To study the drift of a spin packet, a time-resolved Kerr rotation microscope with 3-micron resolution is designed and built. Equipped with a 4-f scanning system, the Kerr rotation microscope can perform spatial scans in a relatively broad area ($100\ \mu m \times 100\ \mu m$).

One possible future plan is to determine the origin of this long-lived spin/valley polarization. As we discussed in the previous chapters, time-resolved measurements

cannot differentiate between resident holes and dark trions. However, resident holes and dark trions have different mass and mobility. Therefore, measuring how fast/far the polarization packet moves could provide us with more information on the long-lived spin/valley polarization in WSe_2.

BIBLIOGRAPHY

BIBLIOGRAPHY

[1] W. Gerlach and O. Stern. *Zeitschrift fur Physik*, 9:349–353, 1922.

[2] I. Zutic and S. Das Sarma. *Rev. Mod. Phys.*, 76:323–410, 2004.

[3] M. Baibich, J. Broto, A. Fert, F. Nguyen Van Dau, F. Petroff, P. Etienne, G. Creuzet, A. Friederich, and J. Chazelas. *Phys. Rev. Lett.*, 61:2472–2475, 1988.

[4] G. Binasch, P. Grunberg, F. Saurenbach, and W. Zinn. *Phys. Rev. B*, 39:4828, 1989.

[5] G. Prinz. *Science*, 282:1660, 1998.

[6] C. Tsang, R. Fontana, T. Lin, D. Heim, V. Speriosu, B. Gurney, and M. Williams. *IEEE Trans. Magn.*, 30:3801, 1994.

[7] M. Dax. *Semicond. Int.*, 20:84, 1997.

[8] *Introduction to Spintronics and Spin Quantum Computation*. University of Maryland (https://www.physics.umd.edu/rgroups/spin/intro.html), retrieved 03/11/2018.

[9] R. J. Elliot. *Phys. Rev.*, 96:266–279, 1954.

[10] Y. Yafet. *Solid State Physics*, volume 14. Academic, New York, 1963.

[11] J. N. Chazalviel. *Phys. Rev. B*, 11:1555–1562, 1975.

[12] G. E. Pikus and A. N. Titkov. *Optical Orientation, Modern Problems in Condensed Matter Science*. North-Holland, Amsterdam, 1984.

[13] A. Kolobov and J. Tominaga. *Two-Dimensional Transition-Metal Dichalcogenides*. Springer, 2016.

[14] *Ann. Phys.*, 526.

[15] J. Padilha, H. Peelaers, A. Janotti, and C. G. Van de Walle. *Phys. Rev. B*, 90:205420, 2014.

[16] K. F. Mak, C. Lee, J. Hone, J. Shan, and T. Heinz. *Phys. Rev. Lett.*, 105:136805, 2010.

[17] D. Xiao, G. Liu, W. Feng, X. Xu, and W. Yao. *Phys. Rev. Lett.*, 108:196802, 2012.

[18] T. Cao, G. Wang, W. Han, H. Ye, C. Zhu, J. Shi, Q. Niu, P. Tan, E. Wang, B. Liu, and J. Feng. *Nat. Commun.*, 3:887, 2012.

[19] *Phys. Rev. B*, 86.

[20] H. Zeng, J. Dai, W. Yao, D. Xiao, and X. Cui. *Nat. Nanotech.*, 7:490–493, 2012.

[21] K. F. Mak, K. he, J. Shan, and T. Heinz. *Nat. Nanotech.*, 7:494–498, 2012.

[22] R. S. Knox. *Theory of Excitons*. Academic Press, New York, 1963.

[23] P. Harrison. *Quantum Well, Wires, and Dots: theoretical and computational physics of semiconductor nanostructures*. Academic Press, New York, 2005.

[24] X. F. He. *Phys. Rev. B*, 43:2063, 1991.

[25] A. Stier, N. Wilson, G. Clark, X. Xu, and S. Crooker. *Nano Lett.*, 16:7054–7060, 2016.

[26] T. Cheiwchanchamnangij and W. R. L. Lambrecht. *Phys. Rev. B*, 85:205302, 2012.

[27] A. T. Hanbicki, M. Currie, G. Kioseoglou, A. L. Friedman, and B. T. Jonker. *Solid State Commun.*, 203:16–20, 2015.

[28] X.-X. Zhang, Y. You, S. Y. F. Zhao, and T. F. Heinz. *Phys. Rev. Lett.*, 115:257403, 2015.

[29] M. Faraday. Experimental researches in electricity. *Philos. Trans. R. Soc. London*, 136:1–20, 1846.

[30] M. Born and E. Wolf. *Principles of Optics*. Cambridge University Press, 1999.

[31] M. Fox. *Optical Properties of Solids*. Oxford University Press, 2001.

[32] C. Jones. *Journal of the Optical Society of America*, 31:488–493, 1941.

[33] J. M. Kikkawa, I. P. Smorchkova, N. Samarth, and D. D. Awschalom. *Science*, 277:1284–1287, 1977.

[34] J. M. Kikkawa and D. D. Awschalom. *Phys. Rev. Lett.*, 80:4313, 1941.

[35] P. A. Bromiley. *Tina Internal Report*, 003, 2003.

[36] T. Yan, X. Qiao, X. Liu, P. Tan, and X Zhang. *Appl. Phys. Lett.*, 105:101901, 2014.

[37] K. P. O'Donnell and Chen X. *Appl. Phys. Lett.*, 58:2924–2926, 1991.

[38] Y.-H. Cho, Gainer G., A. Fischer, J. Song, S. Keller, U. Mishra, and S. DenBaars. *Appl. Phys. Lett.*, 73:1370, 1998.

[39] G. Wang, Bouet L., D. Lagarde, M. Vidal, A. Balocchi, T. Amand, X. Marie, and B. Urbaszek. *Phys. Rev. B*, 90:075413, 2014.

[40] T. Godde, Schmidt D., J. Schmutzler, M. ABmann, J. Debus, F. Withers, E.M. Alexeev, O. Del Pozo-Zamudio, Skrypka O. V., Novoselov K. S., Bayer M., and Tartakovskii A. I. *Phys. Rev. B*, 94:165301, 2016.

[41] J. Huang, T. Hoang, and M. Mikkelsen. *Sci. Rep.*, 6:22414, 2016.

[42] E. Semina, M. Manca, M. Glazov, C. Robert, F. Cadiz, G. Wang, T. Taniguchi, K. Watanabe, M. Pierre, E. Ivchenko, P. Renucci, X. Marie, T. Amand, and B. Urbaszek. *Phys. Rev. B*, 96:085303, 2017.

[43] C. Robert, D. Lagarde, F. Cadiz, G. Wang, B. Lassagne, T. Amand, A. Balocchi, P. Renucci, S. Tongay, B. Urbaszek, and X. Marie. *Phys. Rev. B*, 93:205423, 2016.

[44] A. Kormanyos, V. Zolyomi, N. D. Drummond, P. Rakyta, G. Burkard, and V. I. Fal'ko. *Phys. Rev. B*, 88:045416, 2013.

[45] C. Poellmann, P. Steinleitner, U. Leierseder, G. Plechinger, M. Porer, R. Bratschitsch, C. Schuller, T. Korn, and R. Huber. *Nat. Mat.*, 14:889–893, 2015.

[46] H. Ochoa and R. Roldan. *Phys. Rev. B.*, 87:245421, 2013.

[47] F. Volmer, S. Pissinger, M. Ersfeld, S. Kuhlen, C. Stampfer, and B. Beschoten. *Phys. Rev. B*, 95:235408, 2017.

[48] Z. Ye, T. Cao, K. O'Brien, H. Zhu, X. Yin, Y. Wang, S. G. Louie, and X. Zhang. *Nature*, 513:214, 2014.

[49] X. Zhang, T. Cao, Z. Lu, Y. Lin, F. Zhang, Y. Wang, Z. Li, J. Hone, J. A. Robinson, Dmitry Smirnov, S. G. Louie, and T. F. Heinz. *Nat. Nanotechnol*, 12:883–888, 2017.

[50] P. Dey, L. Yang, C. Robert, G. Wang, B. Urbaszek, X. Marie, and S. A. Crooker. *Phys. Rev. Lett.*, 119:137401, 2017.

[51] A. M. Jones, H. Yu, J. R. Schaibley, J. Yan, D. G. Mandrus, T. Takashi, K. Watanabe, H. Dery, W. Yao, and X. Xu. *Nat. Phys.*, 12:323–327, 2015.

[52] L. Yang, Sinitsyn N. A., W. Chen, J. Yuan, J. Zhang, J. Lou, and S. A. Crooker. *Nat. Phys.*, 11:830–834, 2015.

[53] L. Yang, W. Chen, K. M. McCreary, B. T. Jonker, J. Lou, and S. A. Crooker. *Nano Lett.*, 15:8250–8254, 2015.

[54] E. J. McCormick, M. J. Newburger, Y. K. Luo, K. M. McCreary, Simranjeet. Singh, Iwan. B. Martin, Cichewicz Jr E. J., Jonker B. T., and Kawakami R. K. *2D Mater.*, 5:011010, 2018.

[55] W. Tse, A. Saxena, D. L. Smith, and N. A. Sinitsyn. *Phys. Rev. Lett.*, 113:046602, 2014.

[56] G.-B. Liu, W.-Y. Shan, Y. Yao, W. Yao, and D. Xiao. *Phys. Rev. B.*, 88:085433, 2013.

[57] K. Kosmider, J. W. Gonzalez, and J. Fernandez-Rossier. *Phys. Rev. B.*, 88:245436, 2013.

[58] X. Gu, S. Akturk, and R. Trebino. *Opt. Commun.*, 242:599–604, 2004.